CARMA Memorandum Series #48

CARMA SUMMER SCHOOL 2008

Melvyn Wright, Marc Pound, Dick Plambeck, John Carpenter, Jin Koda, Douglas Bock, Mike Anderson, Shane Bussmann, Joe Converse, Stephanie Cortes, Timothy Davis, Masayuki Fukuhara, Jithin George, Josh Goldstein, Sarah Graves, Nicole Hasler, Amanda Heiderman, David Hogg, Katherine Lee, Timothy Morton, Josep-Maria Masqué, Reiko Momose, Megan Roscioli, Álvaro Sánchez-Monge, Dan Welty, Lei Zhu

August 26, 2008

ABSTRACT

The second CARMA SUMMER SCHOOL was held at the observatory on Cedar Flat 2008 June 23-28 with 20 students from Berkeley, Caltech, Illinois, Maryland, Alabama, Arizona, Texas, England, Spain and Japan. During the school each participant made observations, and analyzed the results. In this memo we collect together some of the results from the student projects.

1. Introduction

The second CARMA SUMMER SCHOOL was held at the observatory on Cedar Flat 2008 June 23-28 with 20 students from Berkeley, Caltech, Illinois, Maryland, Alabama, Arizona, Texas, England, Spain and Japan. During the school each participant made observations and analyzed the results. In this memo we collect together some of the results from the student projects.

The school had the use of the telescope for the week. During the school the students had their own observing projects which they worked on during the week as well as attending lectures and demonstations. Each of the student projects had 5-6 hours of telescope time and the students controlled the telescope for their own projects. The students took the observations, reduced the data and analyzed the results.

On Monday the students learned how to select suitable observing projects for the CARMA telescope. The introductory lectures covered the characteristics of the telescope, instrumentation, and observing techniques. The students learned how to:
1) select suitable astronomical sources for observating.
2) select the observing frequency, spectral lines to be observed.
3) evaluate angular resolution, velocity resolution and sensitivity needed.
4) select the correlator setup and calibrations needed.
5) prepare an observing script to define the observing procedure at the telescope.
6) schedule the telescope and make the observations.

During the rest of the week, the lectures and demonstrations covered the theory and techniques used for millimeter wavelength aperture synthesis and the CARMA array. As they worked on their projects the students learned how to:
7) calibrate the data.
8) make images.
9) analyze and present the results.

On Friday the students made 10-15 minute presentations and we discussed the results. In all, a very satisfying week seeing all the enthusiasm and so many exciting projects from initial planning and observations, to analysis and results.

2. The CARMA Telescope

The CARMA telescope is designed as an aperture synthesis telescope. There are two receiver bands: 3 mm and 1 mm. A basic aperture synthesis observation makes an image the size of the primary beam ($\lambda/D \sim 1'$ at 100 GHz; $0.5'$ at 230 GHz) with a resolution corresponding to the maximum separations of the 15 antennas. You will learn how this works at the school. During the school, the telescope was in a compact antenna configuration, the D-configuration, which gives an angular resolution of $\sim$3-6 at 100 GHz, and 1.5-3$''$ at

230 GHz.

The most convenient source size is one which is smaller than the size of the primary beam when only one pointing is needed. Larger sources can be imaged by time-sharing the pointing of the antennas (mosaicing), at the cost of lowered sensitivity.

The sensitivity is determined by the system noise (receivers plus atmosphere), the bandwidth (or velocity resolution), and the observing time. The atmosphere is usually not so good for 1 mm observations in the summer, or for sources which are at low declinations and must be observed through more of the atmosphere, so it's best to select a bright source which is high in the sky and can be observed at 3 mm, It's best to observe a strong enough source that we can make an image during the school, rather than a detection project, then we can see the effects of different imaging techniques.

Some of the projects that the students wanted to do did not satisfy all these conditions. We put the data on disk where it could be reduced by multiple students, so we could compare the results using different data reduction methods, and the students could work on different types of projects (single pointing, mosaics, continuum, spectral line etc.)

A technical description of the array is at http://cedarflat.mmarray.org/observing/doc/instrument_desc.html and there is a tool to calculate the RMS noise at http://cedarflat.mmarray.org/observing/tools/rms.html .

2.1. Logistics

Because this is a 'hands-on' school, all lectures and demonstrations were held in the control building and at the telescopes at Cedar Flat. Mel, Marc, Dick and nine of the students stayed in the 'Noren' group campground, about 1.5 miles from the control room, and near the antenna pads for the A-configuration. Those who camped avoided the hassle of driving up and down the mountain each day, and had a wonderful opportunity to star-gaze each night. The other students stayed in the dorm and cottage at OVRO. Delicious breakfast, lunch, and dinners were provided at the observatory. We organized a hike to Big Pine Creek on Saturday 28 June.

3. Mike Anderson and Tim Morton (CalTech)

We attempted to detect the cold dust continuum from the galaxy NDWFSJ1431407p330317. This z=0.2 galaxy was detected in X-rays by the Chandra space telescope with an X-ray luminosity of about 10^{43} erg/s, strongly suggesting the presence of an active galactic nucleus (AGN). Subsequent optical follow-up reveals a face-on spiral with no obvious optical emission lines associated with an active galaxy. Assuming the lack of observed AGN emission lines is due to obscuration by dust in this galaxy, we hoped to be able to observe this dust in emission with CARMA. We therefore searched for the dust continuum at 3mm centered about the CO 1-0 line, in order to maximize detection probability.

In five hours of observing time, we found no signal, but were able to place a 1σ upper limit of 0.33 mJy/beam on the emission from this source. Our beam was approximately elliptical with semimajor axis $5.3''$ and semiminor axis $3.7''$ – approximately the same size as the galaxy (a circle with radius of about $5.3''$).

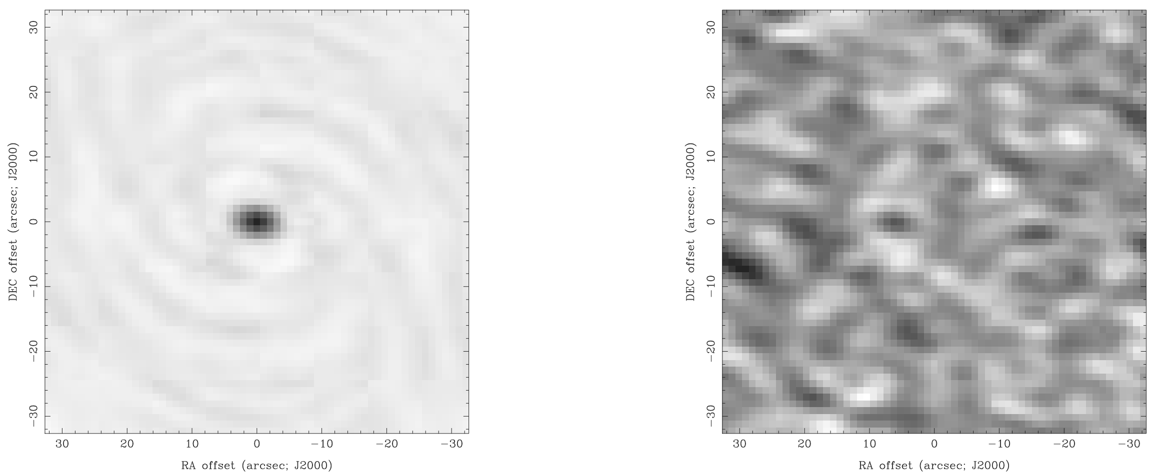

Fig. 1.— Left: This is an image of our beam. Right: This is an image of the source NDWFSJ1431407p330317 created by adding weighted contributions from each channel, over the total bandwidth of 3 Ghz. The rms noise is 0.33 mJy. We find no detections.

Assuming the emission at 3mm is dominated by optically thin dust emission at a uniform temperature, we can apply a modified blackbody spectrum and derive constraints on the dust mass and temperature in this galaxy from our upper limit on the flux. We assume spherical dust grains of radius 0.1 micron and grain density 2 g/cm^3, and assume an extinction coefficient of the form $Q \sim Q_0(2\times10^{14}\mathrm{Hz}/\nu)^{-\alpha}$, where $Q_0 \sim 2$ and $1 < \alpha < 2$. The resulting constraints on the dust mass contained within the beam and the average dust temperature are plotted below. At temperatures below about 5 K, the dust becomes optically thick, but we do not expect an average dust temperature this low.

The constraints are very sensitive to α, but in general the constraints are not very strong unless $\alpha \approx 1$. Thus

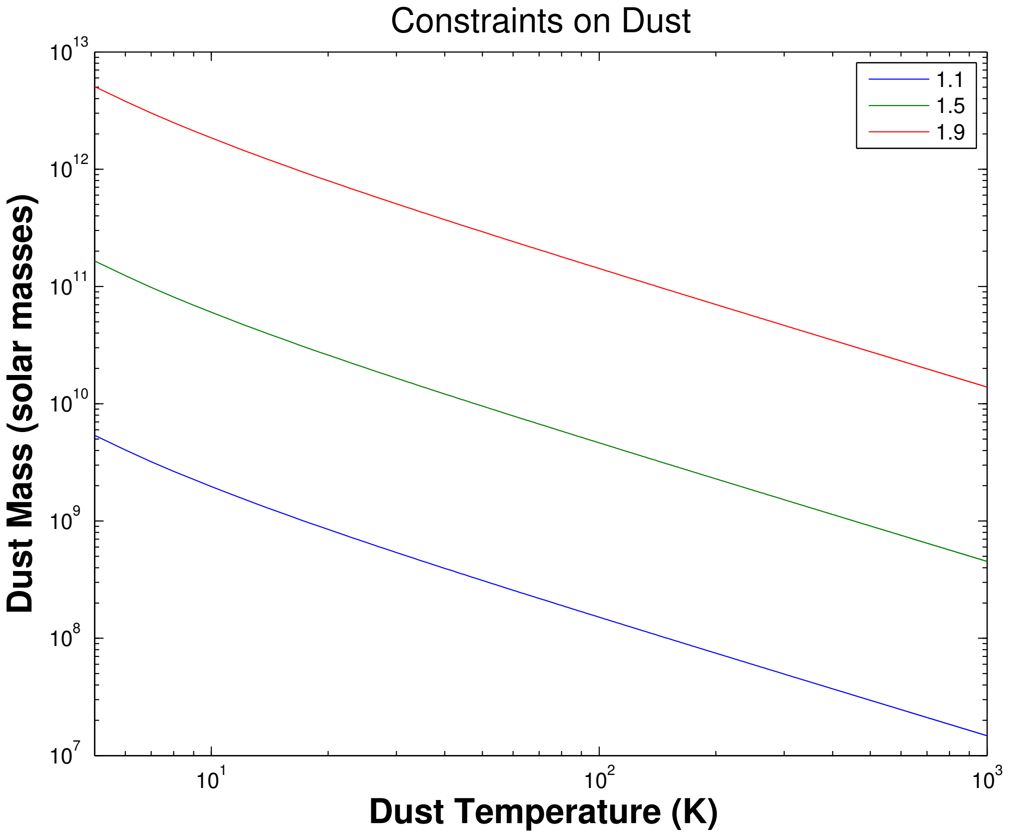

Fig. 2.— Dust Temperature vs. Dust Mass for varying α.

we conclude that obscuration of AGN emission by cold dust is not ruled out by our upper limit. Incidentally, if our observations would have been at 1mm instead of 3mm and we had obtained a similar non-detection, our upper limit on dust mass would have been $\sim 2 \times 10^8$ $M_\odot$ for an α of 1.5–a much stronger limit. Since the total dust mass is likely greater than this, this indicates that we would have had a better shot at detection at this shorter wavelength, despite the increased noise.

We can also use this upper limit to constrain the AGN spectrum. Chandra observations show an x-ray luminosity of 1.0×10^{43} erg/s between 0.5-7 keV. If we assume this x-ray luminosity is dominated by the AGN, then we can test whether the AGN spectrum is flat (i.e. emits the same power at all frequency decades). Over our CARMA bandwidth (3 Ghz), we would expect a minimum total luminosity of 6×10^{40} erg/s emitted by the AGN if its spectral energy distribution (SED) were flat. This corresponds to a measured flux of 1.2 mJy in the central beam. We would have detected such a signal at 4σ confidence, so the lack of a signal suggests the AGN does not have a flat SED from X-ray to microwave.

4. David F. Hogg (Exeter University)

IRAS16293 is a Class 0 proto-binary system in a portion of the Ophiuchus star forming region called L1689. This source has a previously well studied quadrupolar outflow, two bipolar outflows. One of the outflows is E-W and the other NE-SW. As well as these data there is also a clear continuum detection of both components from an OVRO survey that I am working on. In this array configuration the pair was partially resolved in the continuum (Figure 3) and I intend to add this uv data to the already acquired OVRO data to increase the uv coverage of the source.

As well as this the correlator was set up to included 8MHz bands around the 13CO and 18CO lines in an attempt to detect the CO gas in the outflow. Both lines are clearly detected (Figure 4) and appear to trace the dense gas around both stars (Figure 5).

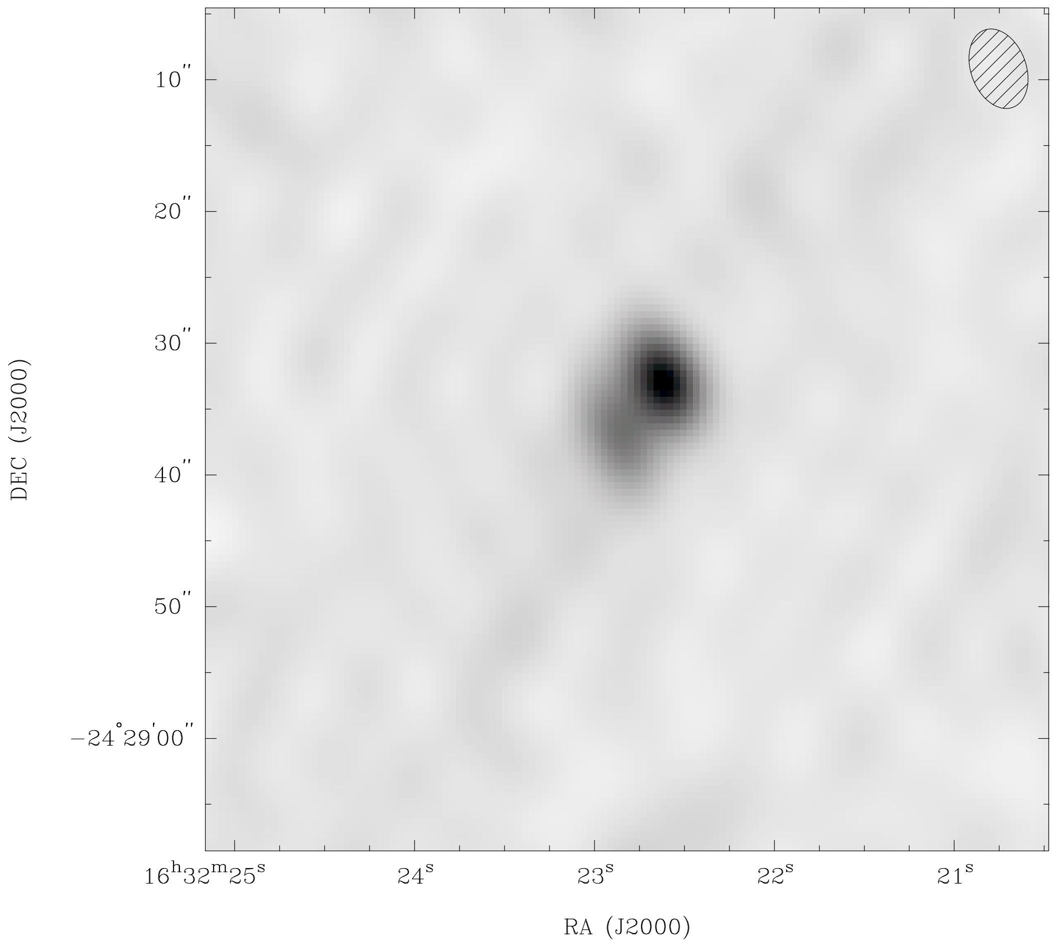

Fig. 3.— Shows the continuum image made of IRAS16293; we clearly detect the dust around both members of the binary.

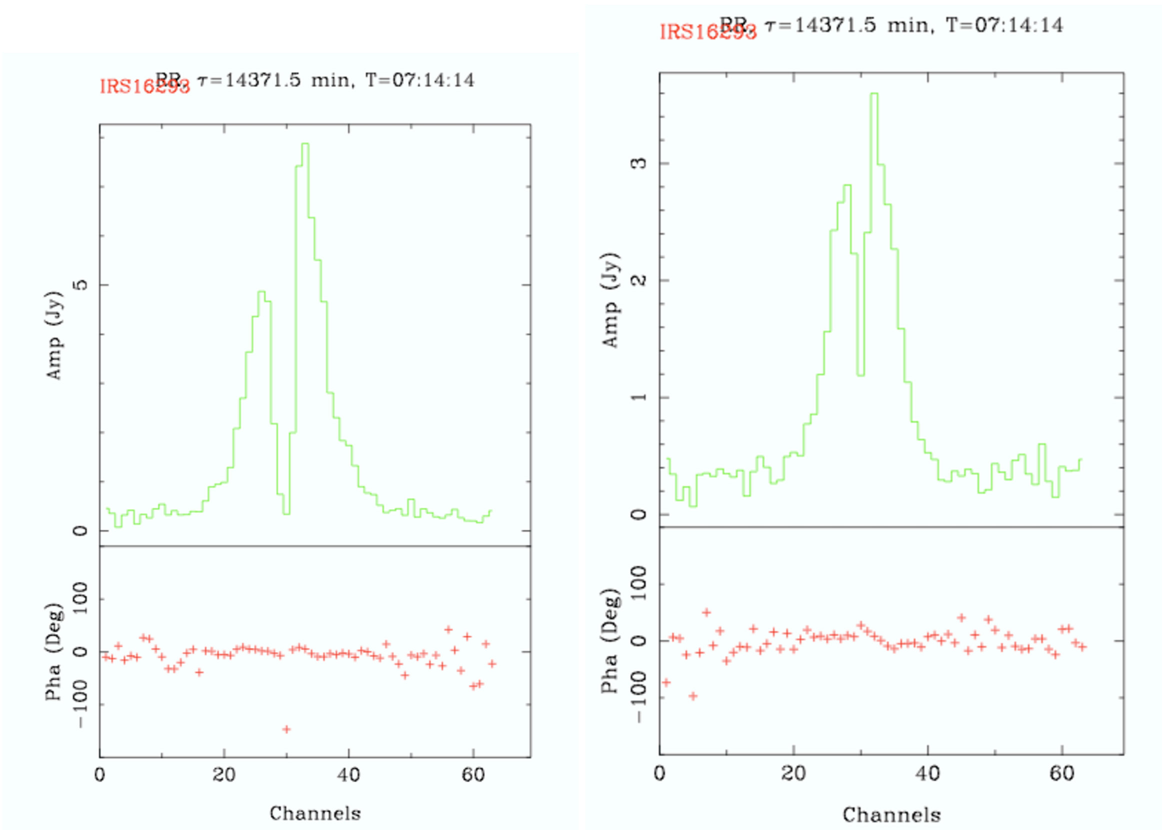

Fig. 4.— IRAS16293 averaged spectra over all baselines for 13CO, left, and C18O, right, we obtain a clear detection of both species with outflow characteristics, one redshifted line and one blueshifted.

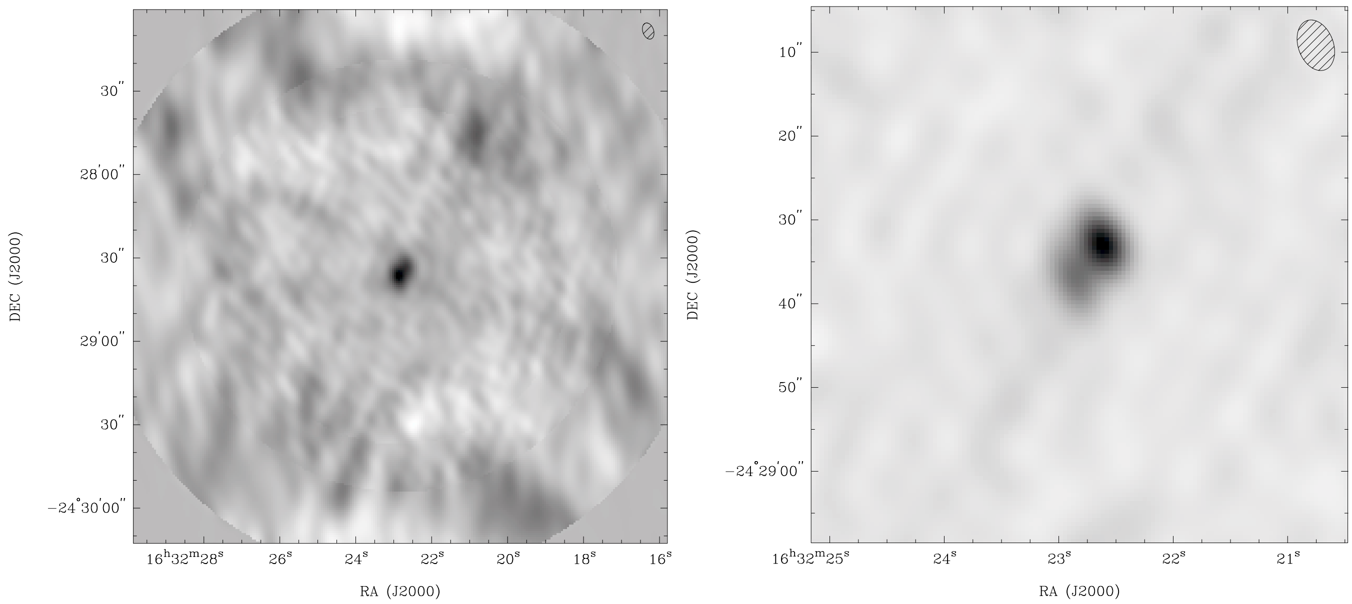

Fig. 5.— IRAS16293 13CO, left, and C18O, right, mapped using all the channels in the above spectra, clearly see the gas very close to the binary pair and there is the possibility the NE-SW outflow is detected in 13CO.

5. Tim Davis (Oxford)

My source was NGC7465, a local elliptical galaxy, that is likely to have undergone a recent merger and starburst. It has a high star formation efficiency, and has known molecular gas. It is part of the ATLAS-3D project, which aims to follow on from SAURON, producing a complete volume limited census of local elliptical galaxies. In further follow on work the gas kinematics will be compared with the star kinematics derived from integral field spectrometry.

I have data from a recent IRAM detection of CO(1-0) in this galaxy, which suggests a linewidth of $\simeq$250km/s and a flux at peak of 0.5 Jy. As such I observed 3mm, CO(1-0), in the 62-62-62 correlator setup.

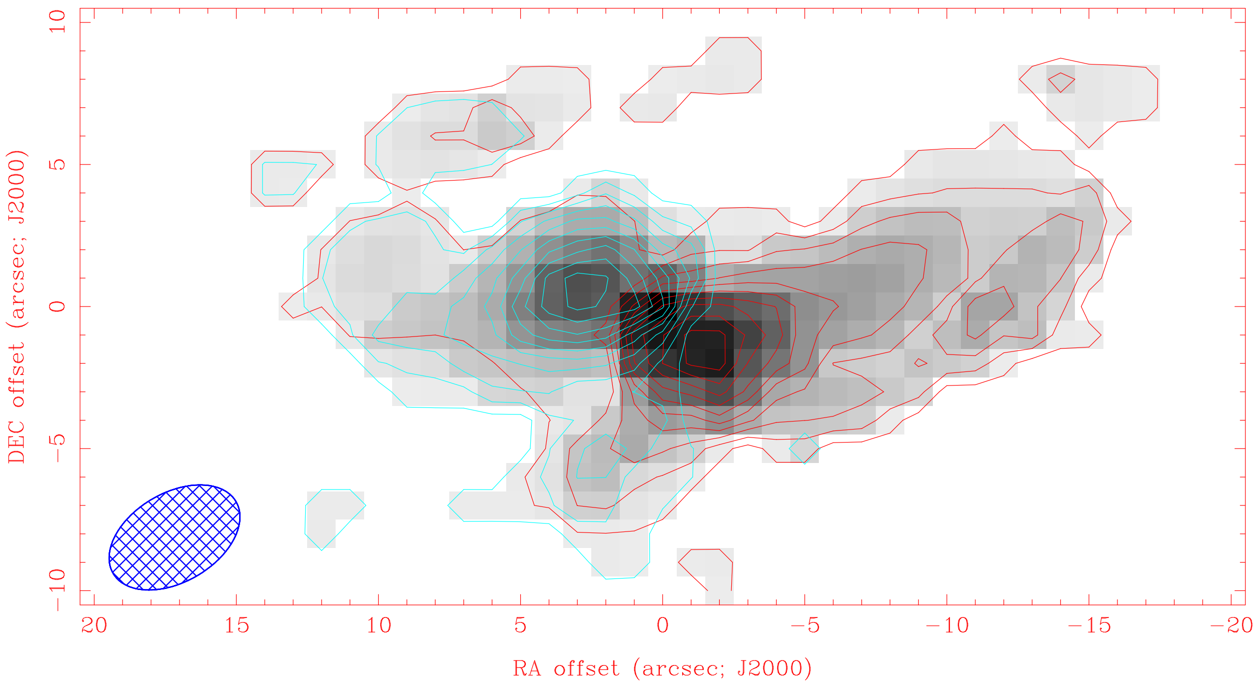

Fig. 6.— CARMA map of the CO(1-0) transition in the center of NGC7465. The gas is highly compact, covering an area 30″ by 5″. Red contours are redshifted gas, blue is blueshifted. The gas seems to have rotation anti-clockwise on this figure.

As shown in the figures, coherent rotation of a disc of gas was detected. The maximum disc rotation velocity was 80 km/s. The galaxy has a flat rotation curve of 10km/s, suggesting the gas rotates faster than the stars around it.

The approximately Keplerian velocity distribution detected allows the mass of the central black hole to be estimated. The value obtained was 2x10^8 $M_\odot$. Relations between black hole mass and galaxy mass have been used to estimate the total galaxy mass as 10^{12} $M_\odot$.

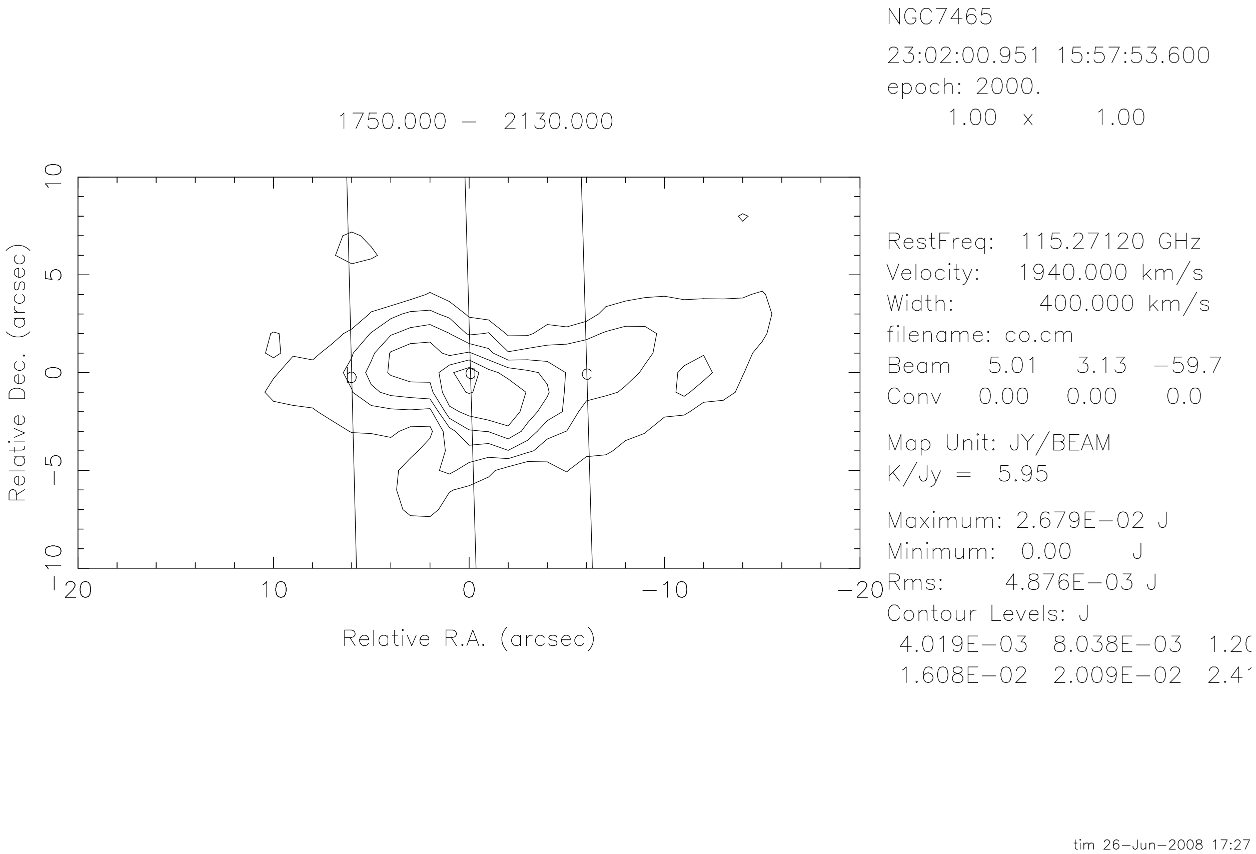

Fig. 7.— Line *a* on this plot represents the derived rotation axis. All three lines are plotted in the next figure to enable the morphology of the gas to be determined.

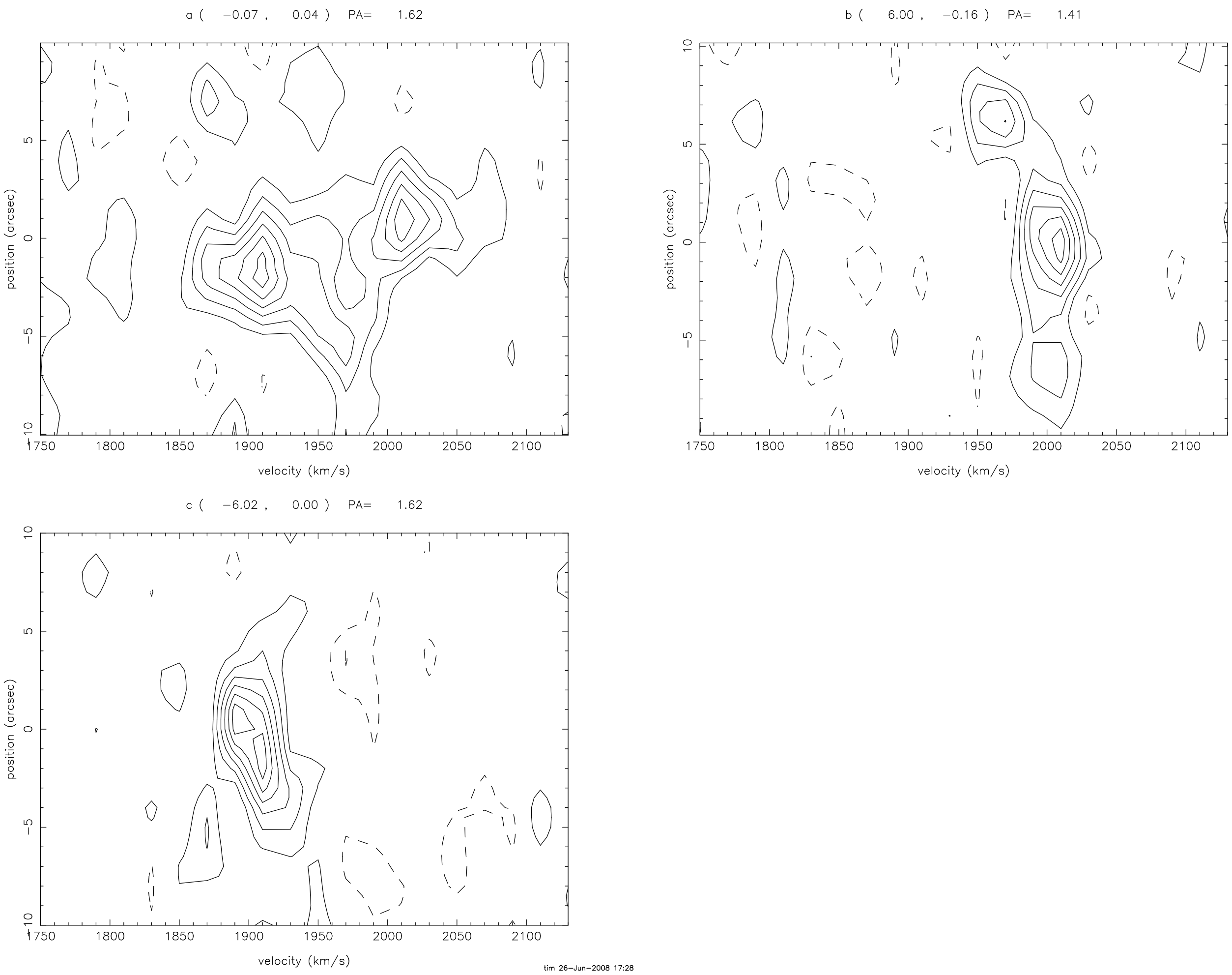

Fig. 8.— The three velocity-position plots for the lines shown across in the previous figure. They provide solid evidence for the rotation axis shown, and show coherent rotation. The first plot shows a cut through the rotation axis, and the blue and red shifted areas suggest a disc morphology is most likely.

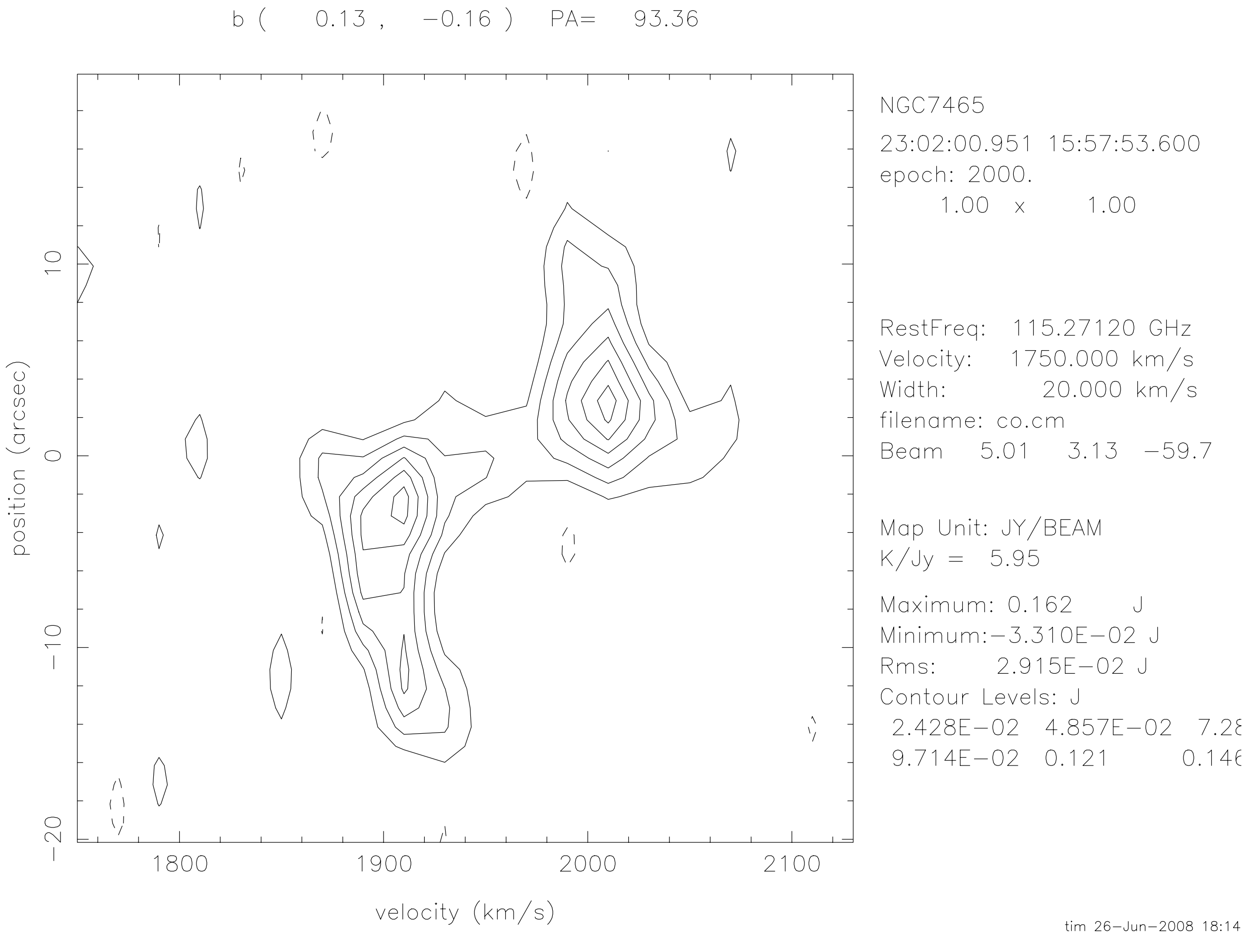

Fig. 9.— A position velocity slice through the disc shows a possible Keplerian velocity distribution.

6. Sarah Graves (Cambridge)

The source being observed was V380 Ori NE, a bipolar molecular outflow around a class 0/I protostar, near L1641-N in the Orion molecular cloud. It is orientated North-South along the plane of the sky, allowing the separate red and blue bipolar outflow to be easily seen. This observation detected CO 1—0 emission from the molecular outflow, allowing the structure of the outflow to be examined.

It was observed using two 7 point mosaics, one centered on the center of the outflow (RA 05:36:36.0, Dec -06:38:57), and one centered half a beam FWHM north. One narrow band (31Mhz) was used centered on CO 1-0, as well as two 500MHz wide bands. The source has an ambient of velocity of 8 km/s LSR.

The red and blue shifted gas is shown in Figure 10 tracing a bipolar outflow structure, roughly centered on the continuum source.

Channel maps of the data show the manner in which different velocities of gas show different structures. The slower moving gas shows a wide outflow structure, changing to a narrower structure in the faster moving gas. This is consistent with the model of molecular gas being entrained by a jet from the protostar. The very narrow gas structures visible in the high speed gas suggests that this is gas that has been caught up in the gas itself. At the ambient velocity of the gas (around 8 km/s) there is no clear structure.

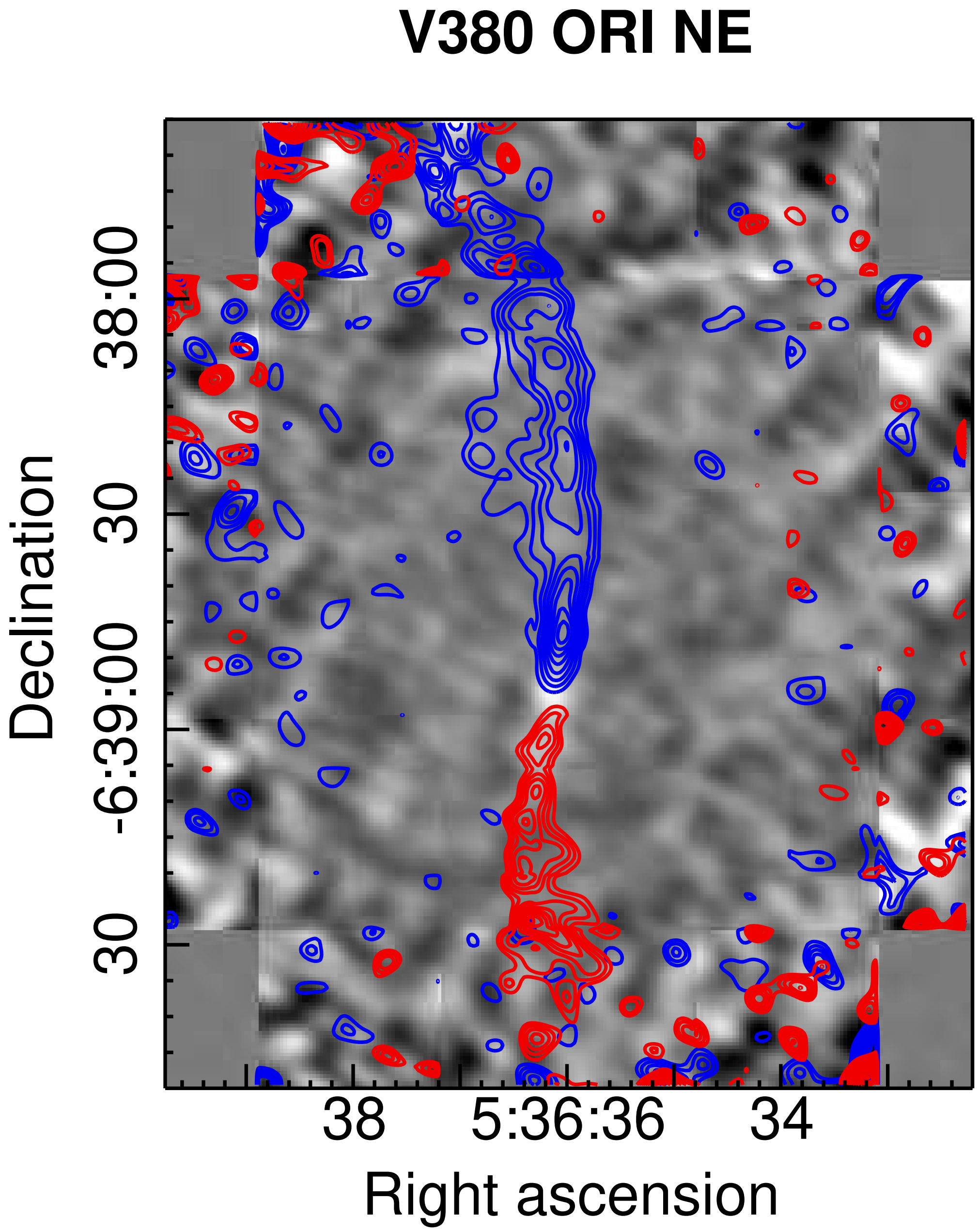

Fig. 10.— Blue and red shifted emmision integrated from approx. -5 to 6 and 10 to 17 km/s, overlain on the wideband continuum emission.

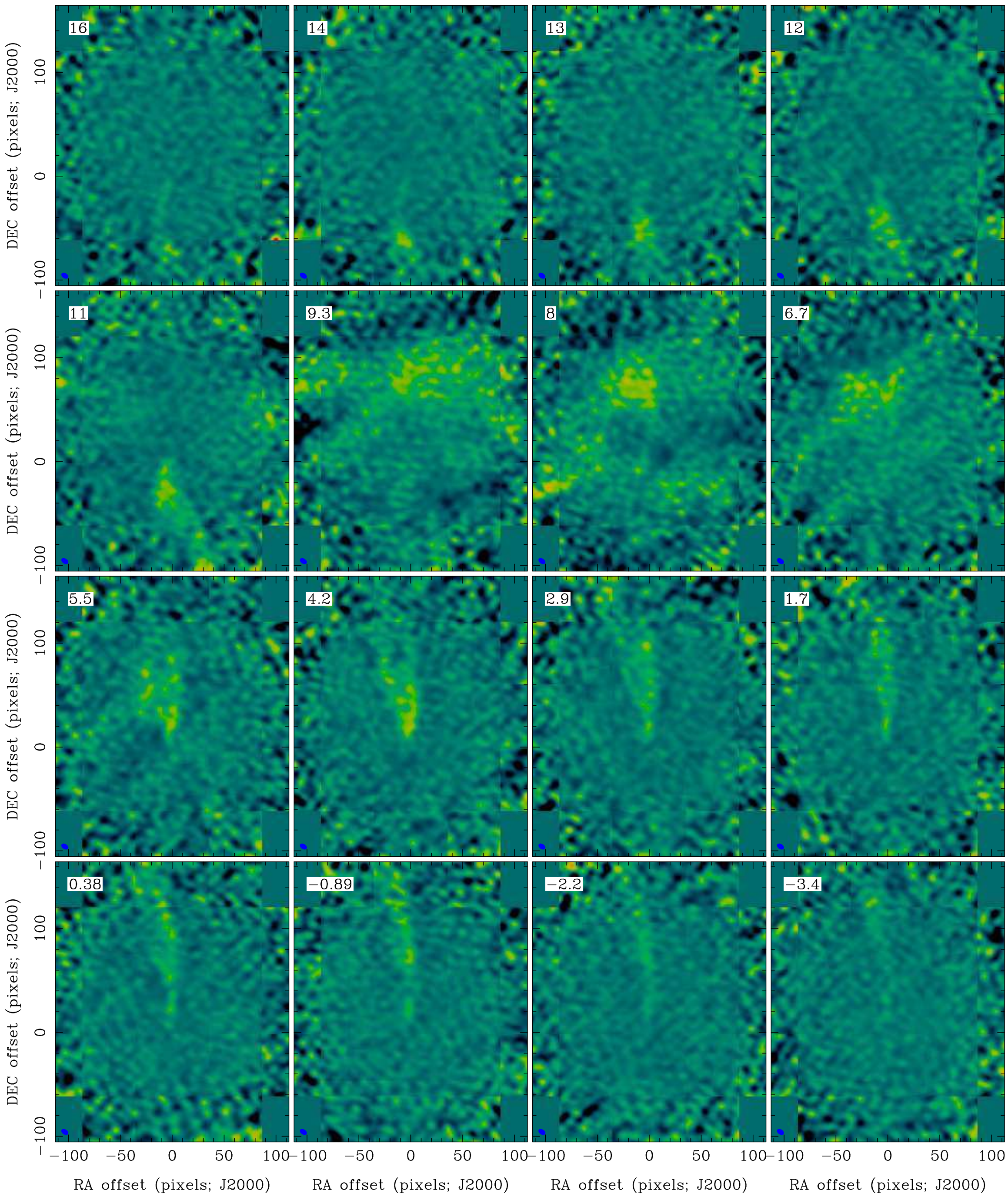

Fig. 11.— The 1.7 km/s wide channel data, from high velocity to low velocity. A cross marks the postion of the V380Ori-NE outflow source, taken from Davis, C.J. et al 2000, MNRAS.

7. Josh Goldstein and Jithin George (UMD)

We observe CN and CO in IRC+10216, an AGB star surrounded by a shell of expanding gas. The CO ring was previously observed with the BIMA antennas (Fong et al 2006, ApJ, 652, 1626). The CN 2-1 transition at a frequency of 226.9 GHz has also observed for this source with the Plateau de Bure interferometer (Lucas, et al. 1995, Ap&SS, 224, 293).

A waffle pattern is present throughout all of our data (Fig. 12), possibly due either to poor uv coverage or fringe effects from our 19 point mosaic. We attempted to model this by convolving Cas A, which has a structure approximating the CN ring, by the beam (Fig. 13). Unfortunately deconvolving the data using this model is unsuccessful. We instead ignore the large-scale waffle effect and clean in a tight region around the emission.

We are able to successfully resolve the CN 1-0 line at 113.49 GHz. The result is an expanding ring centered at a velocity of -26 km/sec and a line width of 30 km/sec (Fig. 14). The moment map (Fig. 15) yields a good spatial comparison with the 2-1 line observation (Lucas et al., Fig. 1). In the CO 1-0 transition, observed with a 31 MHz correlator, we detect only the central brightness peak (Fig. 16) and see none of the extended structure of Fong et al. We also merged our observations with single dish data also taken during the summer school (Fig. 17,18).

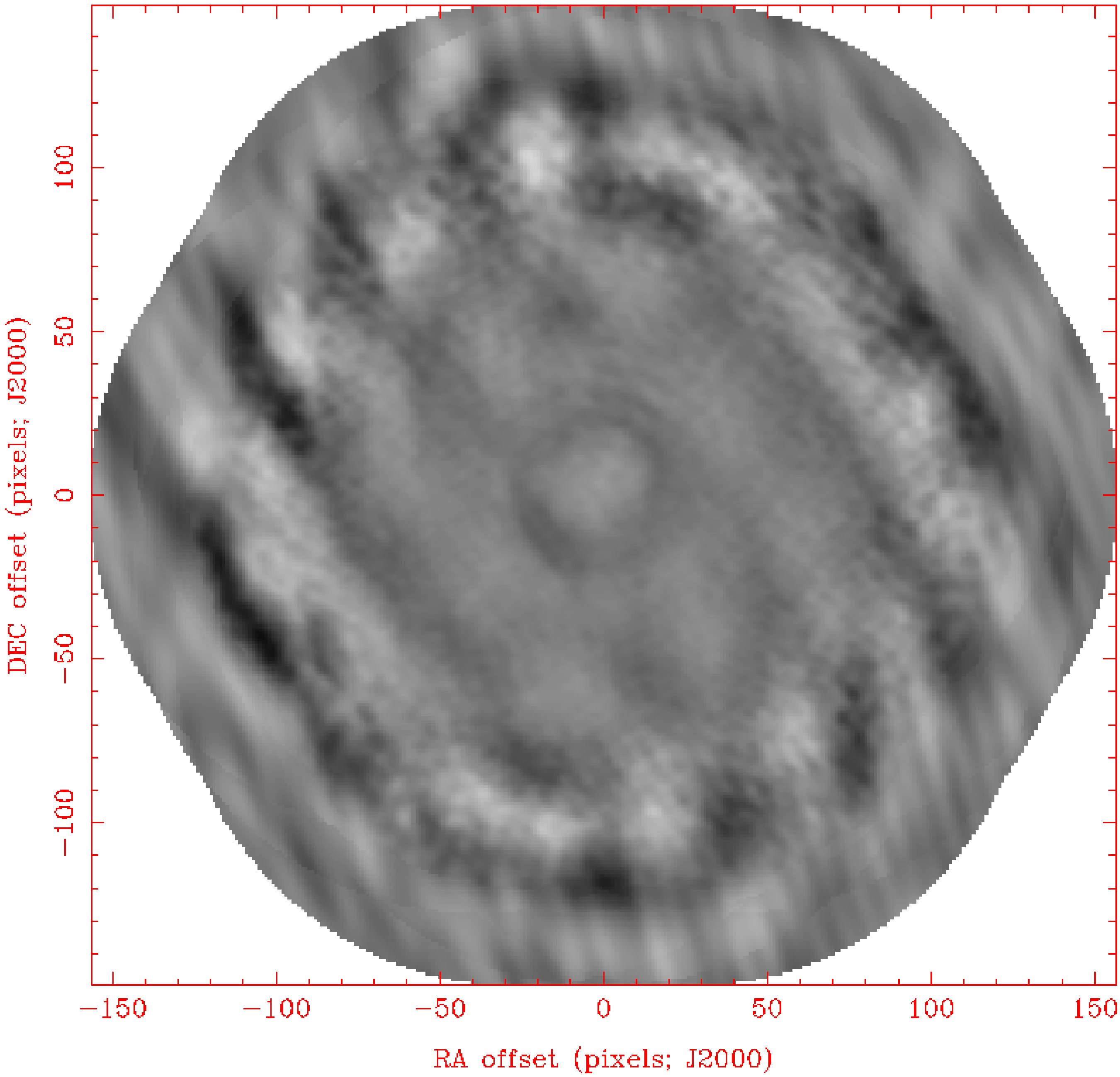

Fig. 12.— Waffle-like structure in the mosaic CN dirty map of IRC+10216

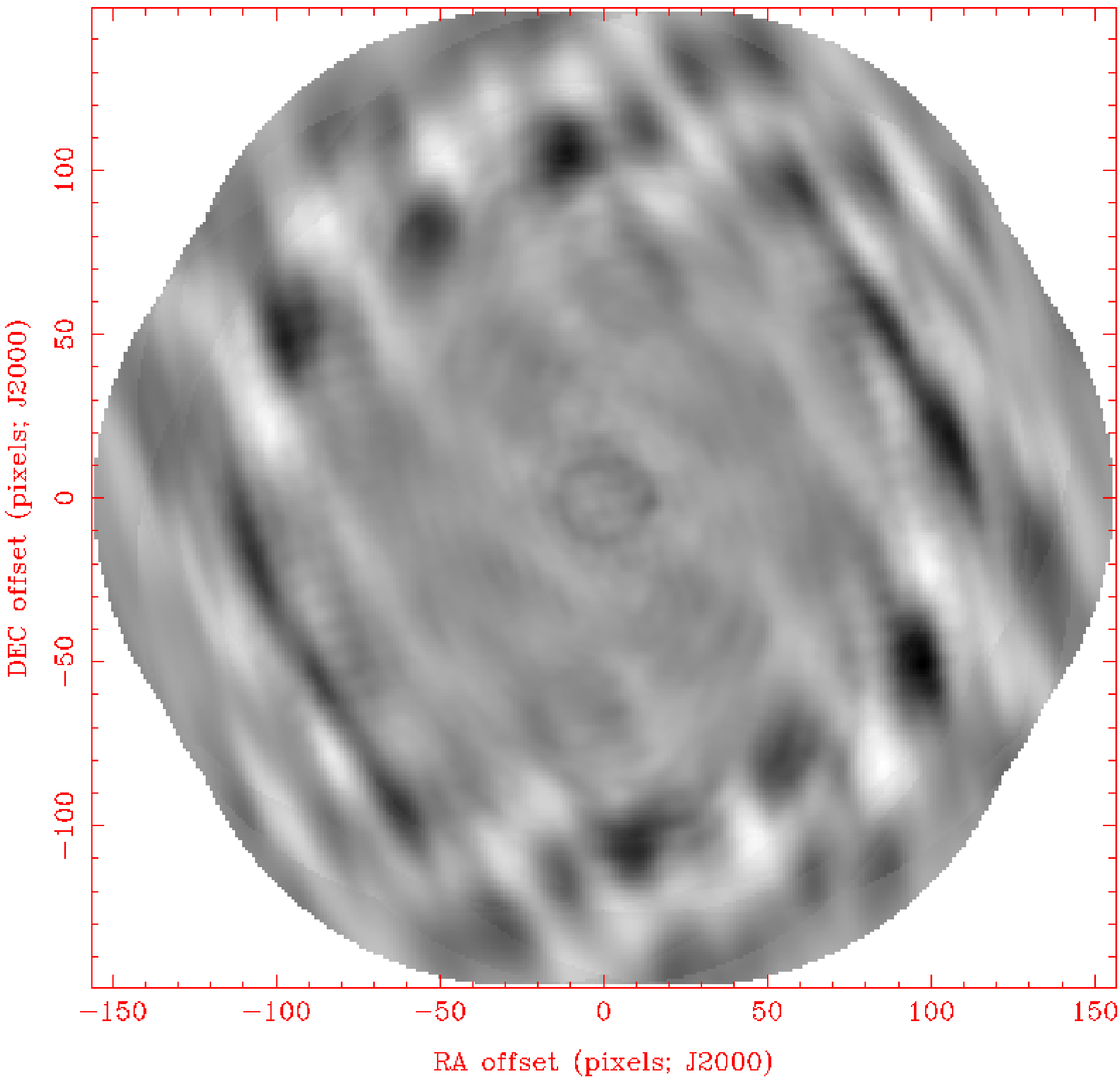

Fig. 13.— Cas A model convolved with the uv-sampling for the 19 point mosaic of IRC+10216.

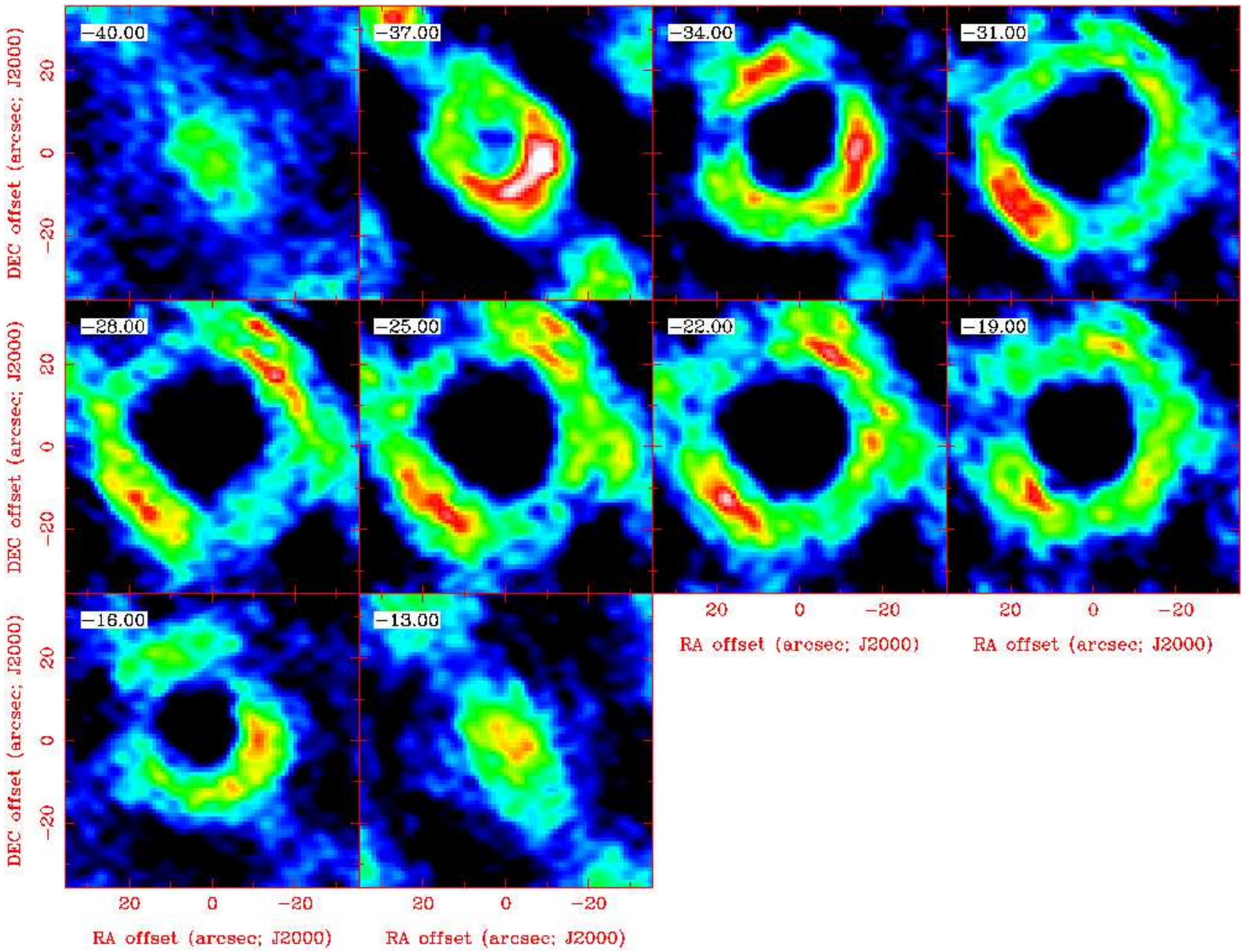

Fig. 14.— CN emission around IRC+10216 by channel. The channel maps have 3 km/s widths.

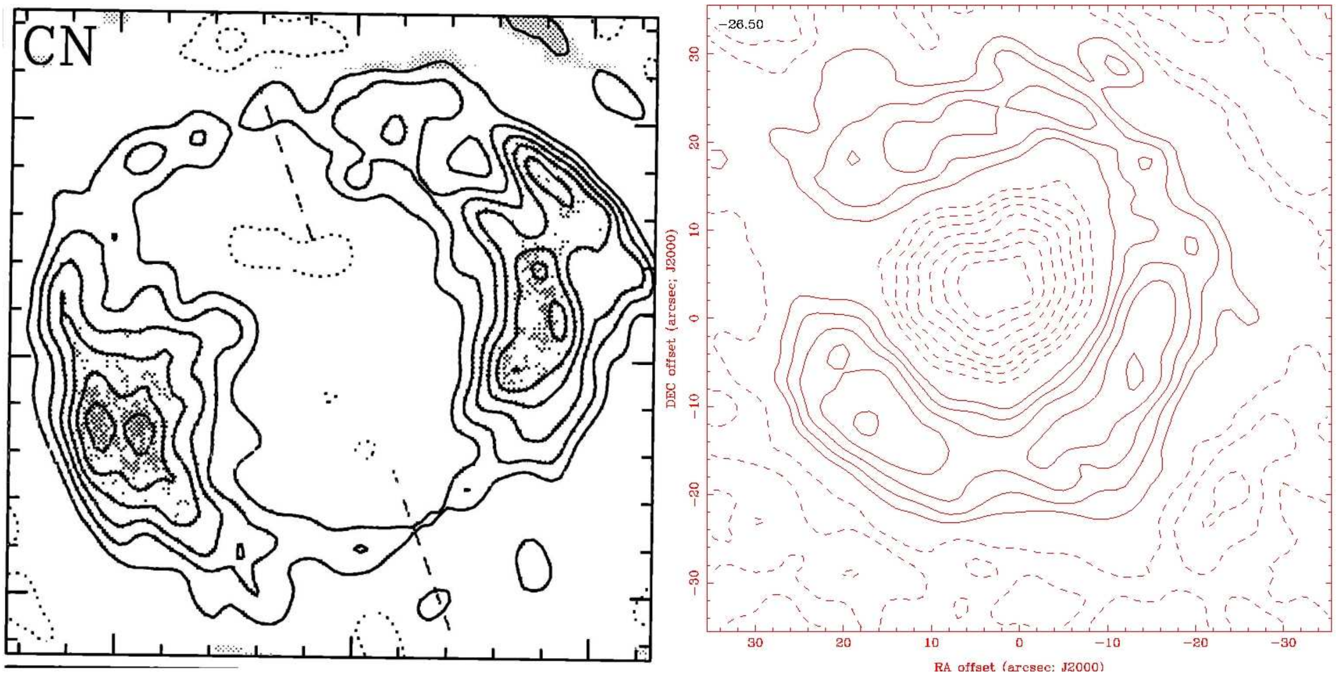

Fig. 15.— Moment map of CN(1-0) emission around IRC+10216 (right) compared to the CN(2-1) line observation from Plateu de Bure (left).

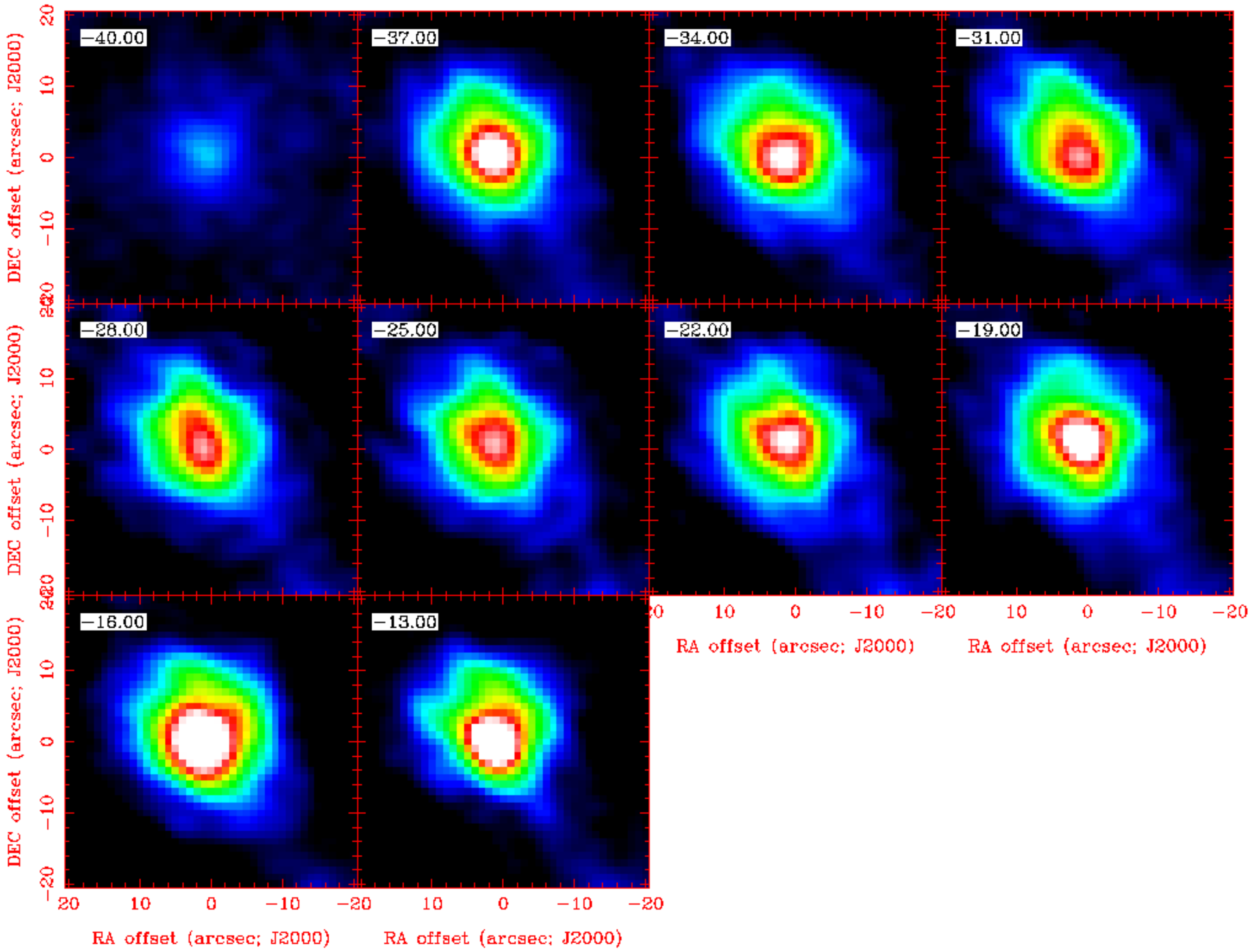

Fig. 16.— Channel maps of CO emission in IRC+10216, with widths of 3 km/s.

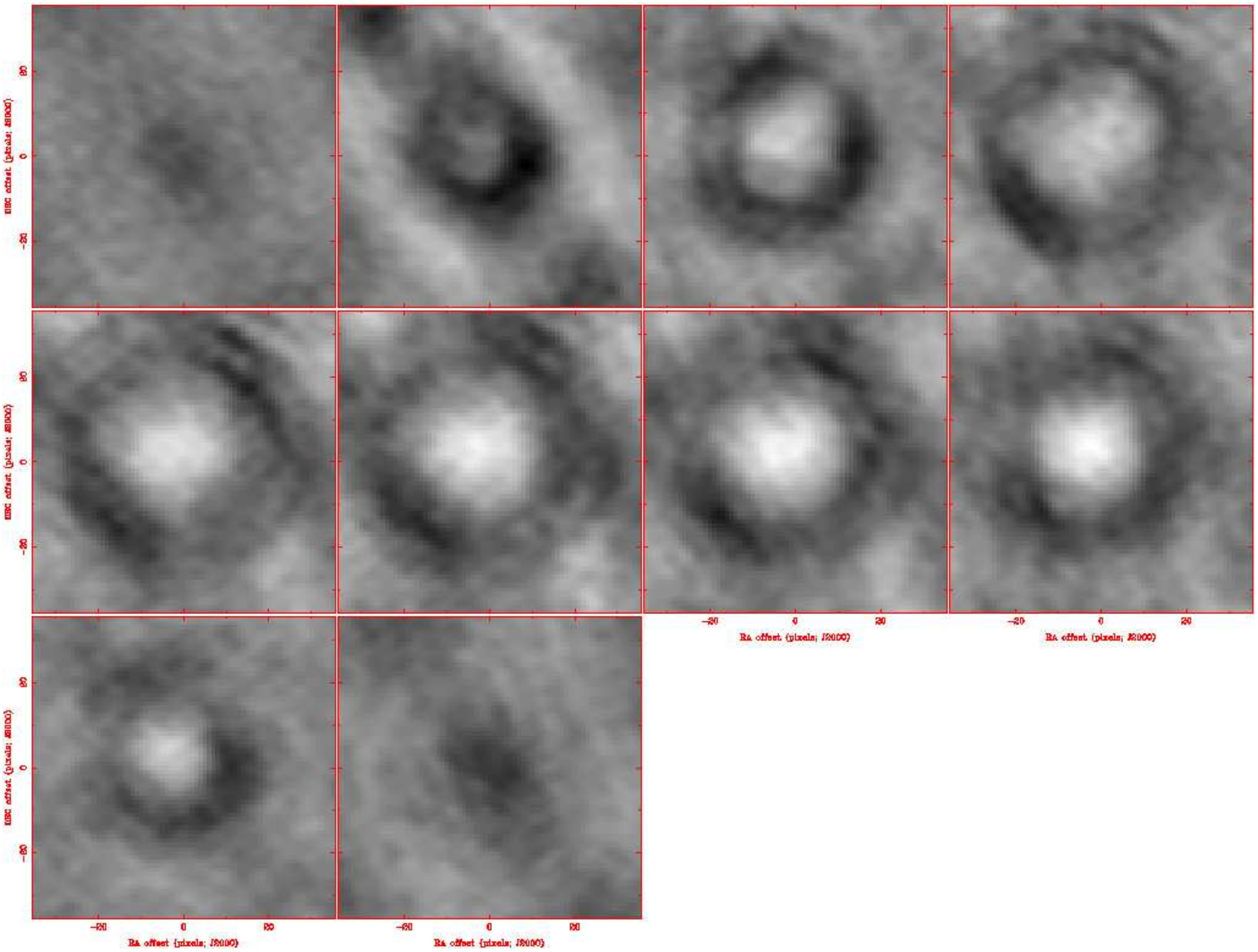

Fig. 17.— Single dish and mosaic data merged: IRC+10216 CN map

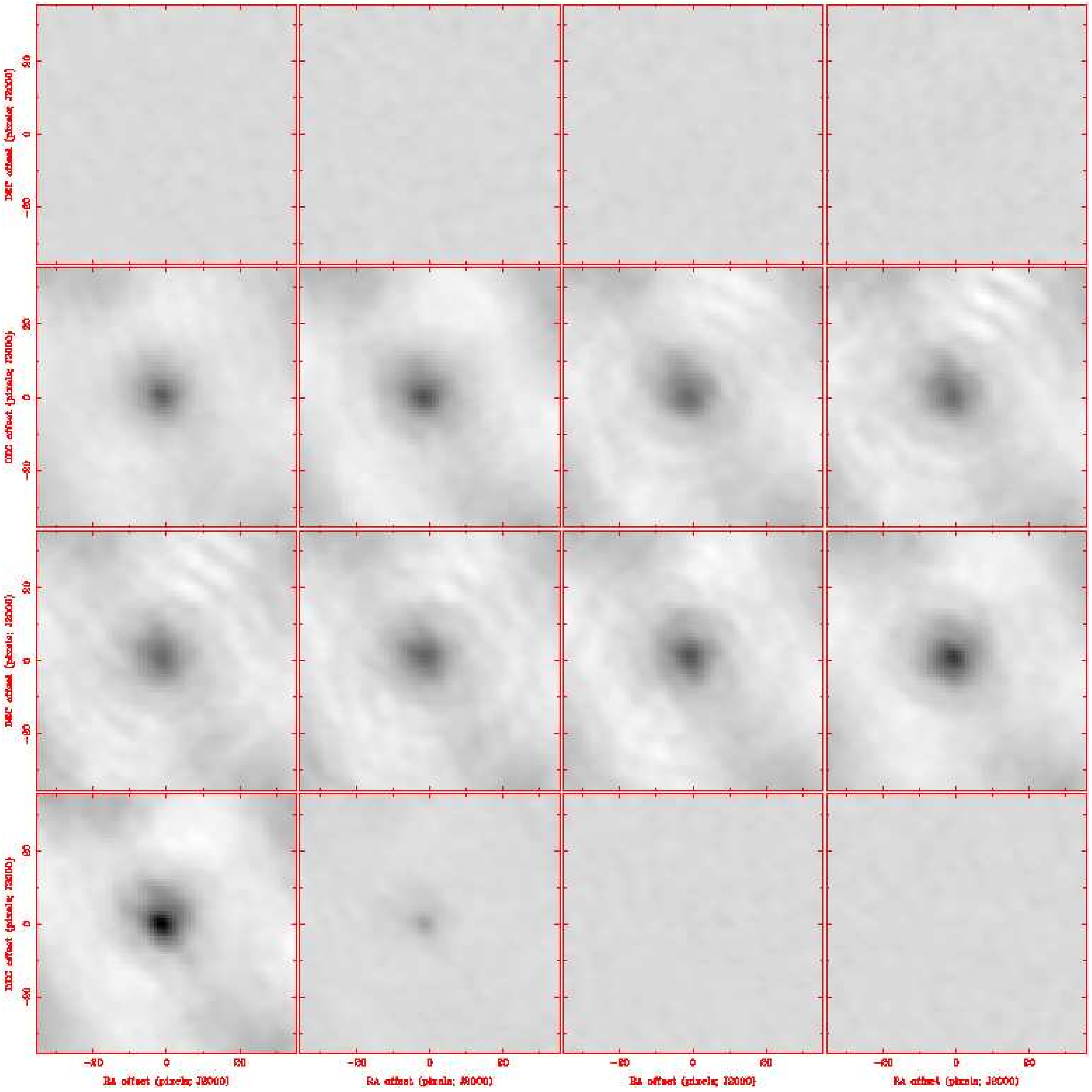

Fig. 18.— Single dish and mosaic data merged: IRC+10216 CO map

8. Shane Bussmann (University of Arizona)

This pedagogical project is aimed at mapping the central 75″ of the nearby bright galaxy NGC 253 in the HCN(1-0) transition. Lying at a distance of $\sim$ 4 Mpc, this corresponds to the central 1.5 kpc with a spatial resolution of approximately 0.15 kpc in the D array configuration of CARMA. Knudsen et al. (2007) mapped HCN(1-0) emission with the Owens Valley Radio Observatory and identified significant structure on these scales. The synthesized beam of this project will have a size of about 10.5″ by 6″. In comparison, the data from Knudsen et al. (2007) have a resolution of 3.9″ by 2.7″. Although the spatial resolution of this project is not as good, it should be sufficient to identify the extended nature of the HCN(1-0) emission in the central kpc of this object. NGC 253 will serve as an excellent target since the primary goal of this project is to obtain a high S/N image (preferably of an extended object) and understand how different methods in the data reduction process affect the results.

NGC 253 is a nearby (d $\sim$ 3.5 Mpc) starbursting SAB galaxy that is known to be extremely bright in HCN (1-0). Knudsen et al. (2007) mapped the central kpc of this object with the OVRO C and E array configurations in a variety of molecular transitions, including HCN (1-0), with $\sim$60 pc resolution. HCN is a useful transition to observe because it is a tracer of the dense molecular gas (critical density for excitation is $\sim 10^6$ cm^{-3}) that is a prerequisite for star-formation.

With mm-wavelength interferometers, it is possible to resolve the spatial and spectral structure of the molecular line emission in nearby galaxies like NGC 253. Knudsen et al. (2007) presented a $\sim$40x30″ map of NGC 253 centered on the nucleus and covering the velocity range 89 km s^{-1} to 401 km s^{-1} in binsizes of 14 km s^{-1}. These authors identified the signature of a rotation curve, in the sense that the centroid of the blue-shifted emission is offset approximately 10″ to the northeast, while the centroid of the red-shifted emission is offset in the opposite direction.

In Figure 19, we present channel maps of NGC 253 obtained with CARMA. Our spatial and spectral resolution are degraded compared to the data presented by Knudsen et al. (2007), but we find similar results. Our synthesized beam (shown with the blue oval in the lower left corner of each channel map) has a FWHM of $\approx$7″, which corresponds to a physical size of 120 pc. We used the 15 channel, 500MHz configuration for the first spectral window and the 63 channel, 62 MHz configuration for the next two windows. Figure 19 shows that from 150 to 250 km s^{-1}, extended emission is seen approximately 10″ to the northeast, while from 260 to 330 km s^{-1}, emission is seen approximately 10″ to the southwest.

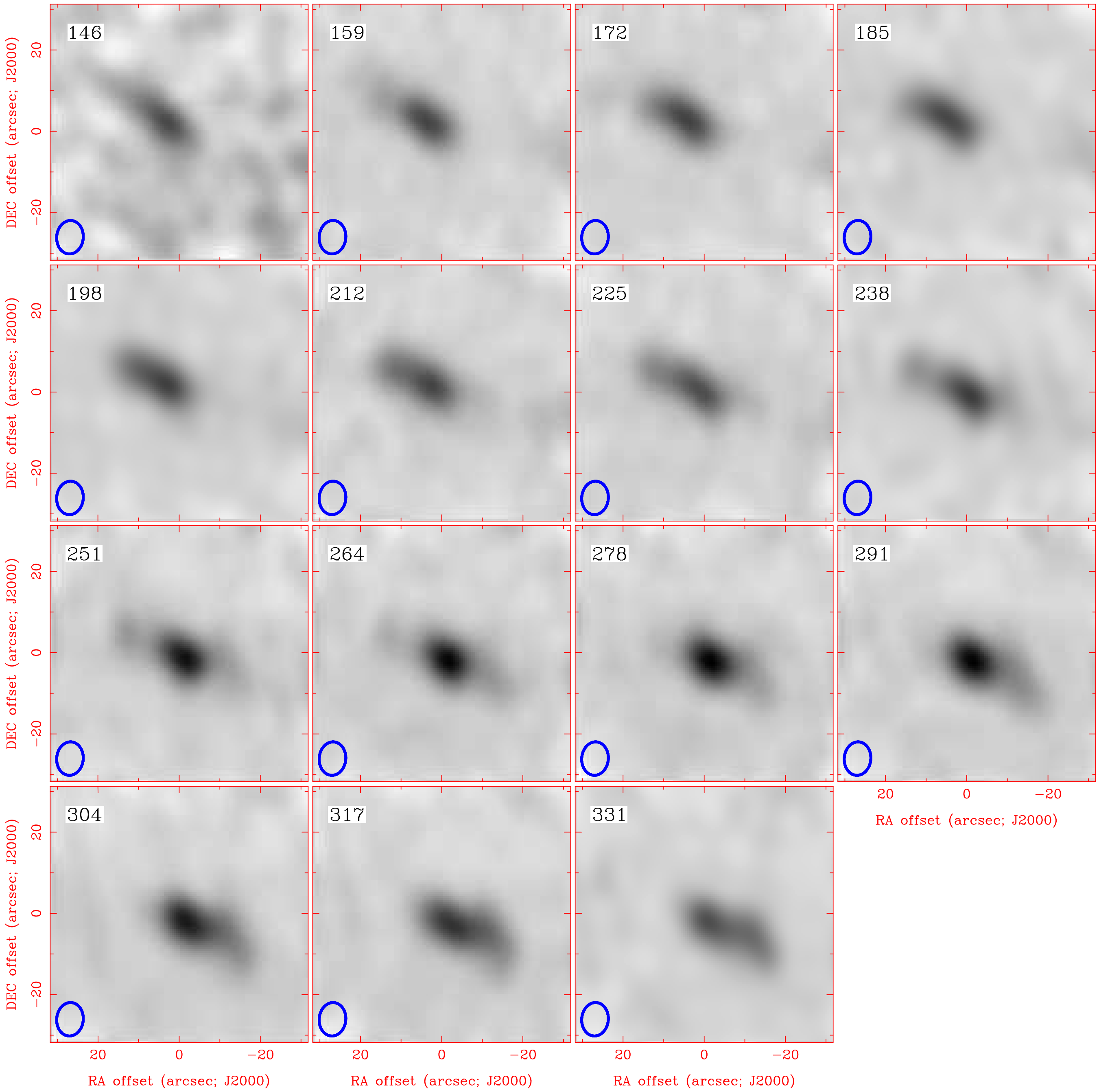

Fig. 19.— Channel map of HCN(1-0) emission from NGC 253. Blue oval shows size and shape of synthesized beam. Top left corner of each channel map shows the central velocity in that bin.

9. Stephanie Cortes (University of Arizona)

L1551 IRS 5 is a multiple proto-stellar system from which a large ($\sim$20′) outflow originates. Lim & Takakuwa (2006) have resolved the compact sources into three components, each with a protostellar disk ($\sim$0.1″) embedded within an envelope. We observed L1551 IRS 5 in the CARMA D-configuration to search for signs of outflow or envelope rotation using ^{12}CO, ^{13}CO, C^{17}O, and map the continuum emission at 3mm. Later we hope to combine our map in the D-configuration with the CARMA C-configuration to produce a combined map over a wider range in resolutions from the compact disk to the extended envelope emission, possibly including the base of the outflows.

Figure 20 shows the 3mm resolved continuum image. The total flux density is 0.5 Jy $\pm$ 2.5 mJy, measured with the MIRIAD task UVFIT and assuming a Gaussian profile. The source size is 3.5$\times$3.0″, which is approximately 480$\times$560 AU at the distance of L1551 IRS 5. Figure 21 shows the spectral lines observed, all with a velocity resolution of 0.4 km/s. It appears that all three species originate from extended structure, rather than compact structure. Several different velocity components are visible in the channel maps, although there is probably sidelobe contamination that is making the mapping challenging. The different velocity components may be coming from a combination of outflows, random motions within the cloud, or rotation of the envelope. Further analysis may be carried out later.

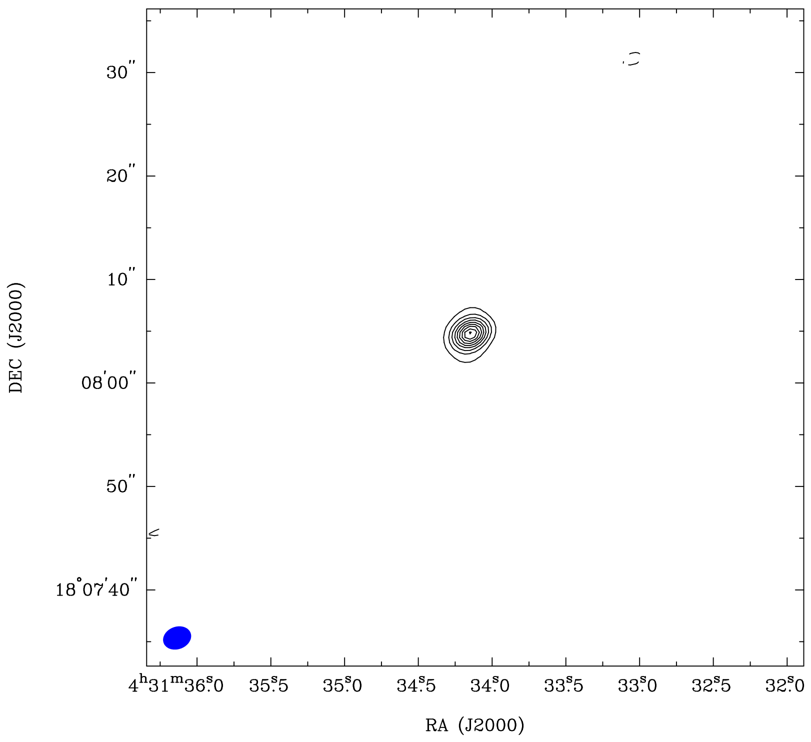

Fig. 20.— Continuum at 3mm, arising predominantly from dust in the disk-envelope system. The contours are plotted at nσ where σ=5.6 mJy and n=-2,3,5,7,...19.

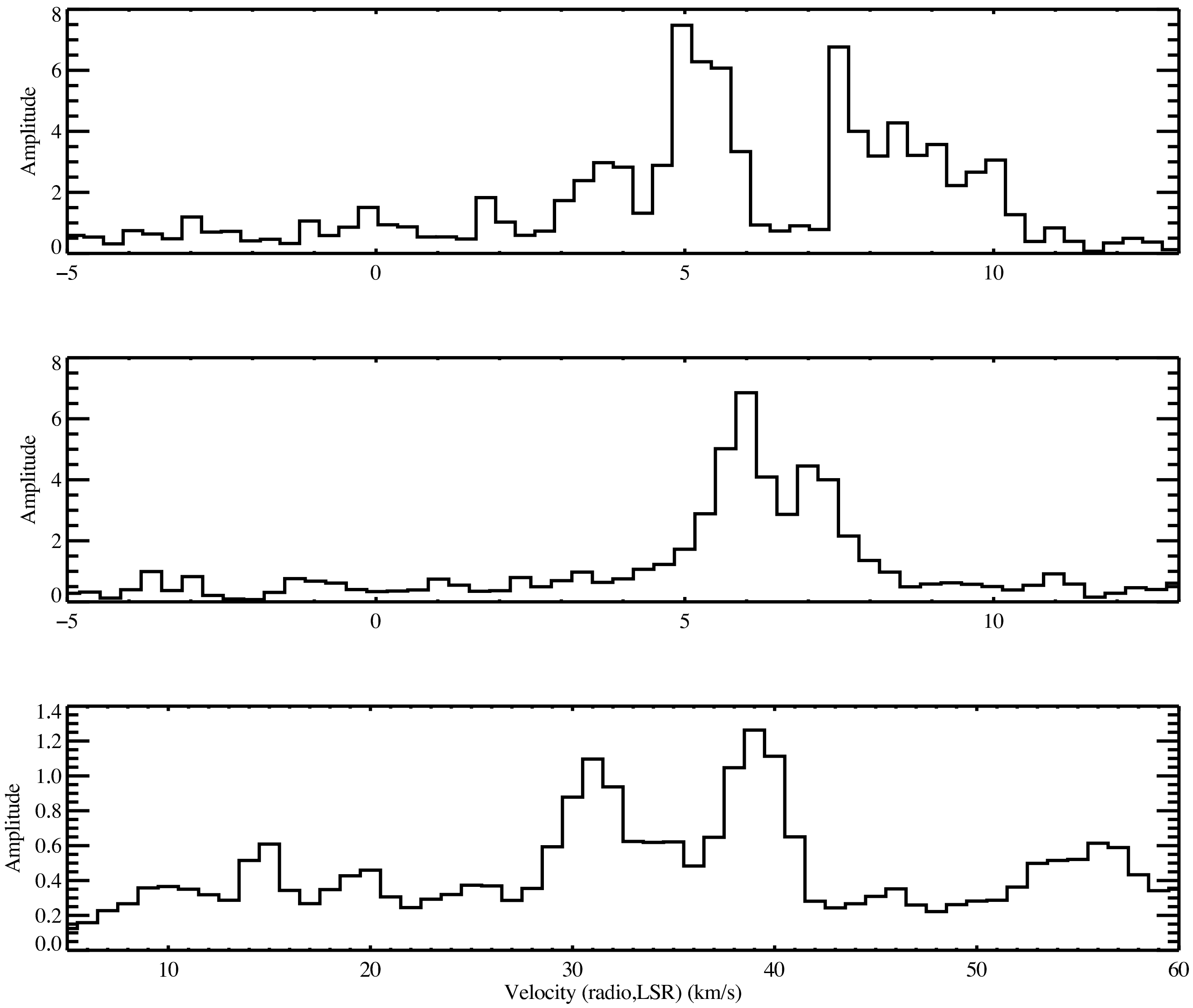

Fig. 21.— The ^{12}CO (top) emission is coming predominantly from baselines shorter than 15 kλ, while the ^{13}CO (middle) emission comes from baselines shorter than 20 kλ, and the $C^{17}O$ (bottom) emission arises from baselines shorter than 35 kλ.

10. Dan Welty (UIUC)

Several generations of star formation are thought to have taken place in the Cep OB2 region. CO observations of the region have revealed a series of globules associated with the diffuse H II region IC 1396. The globules are arranged in a roughly elliptical, apparently expanding ring around the exciting O6 star HD 206267. A number of the globules appear to be associated with IRAS point sources consistent with young stellar objects – which may represent the third generation of star formation in the region. Higher resolution observations of the globule nearest HD 206267 revealed a bright, dense rim structure oriented toward the star; the gas appears to have been compressed by strong UV radiation and/or winds from HD 206267.

We mapped a second, more distant globule (one of those containing a possible YSO) in ^{12CO}, in order to further investigate the interaction between HD 206267 and the remnant molecular material. Because the globule is of order 2 arcmin in diameter, we used a 37-point hexagonal grid, on 30″ centers, to construct a mosaic roughly 3 arcmin in diameter. In addition, we inserted periodic observations of a "blank" field 8 arcmin away in an attempt to use the autocorrelation data from the individual antennas in the array to simulate a "single-dish" configuration whose data could be combined with the interferometric data from the array.

CO is clearly detected in the "single-dish" data, in a strong, narrow component at -4 km s^{-1} which shows strong variations across the globule. Several weaker components, showing less variation, are also detected. The next steps are to obtain maps and spectra from the interferometric data and then to combine the two data sets.

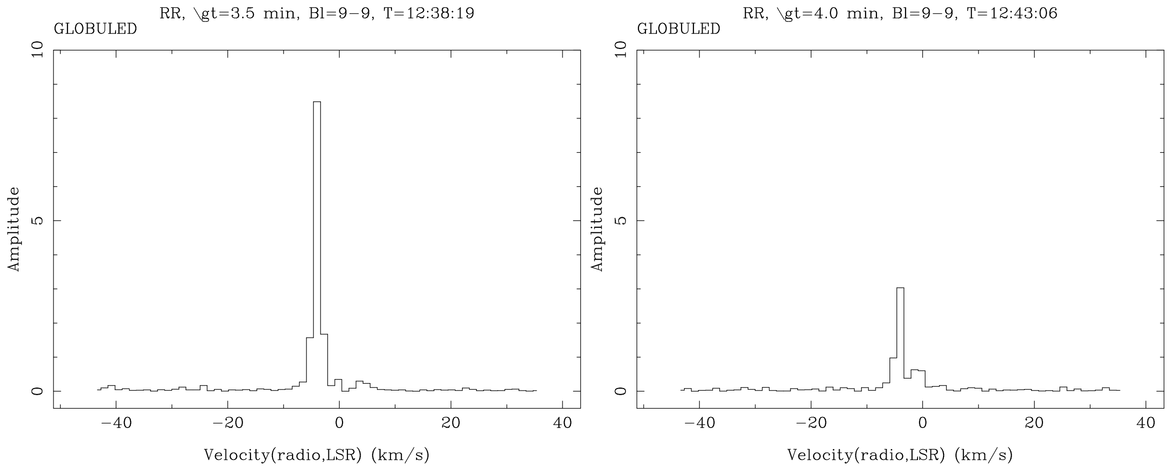

Fig. 22.— ^{12}CO emission near the center (*top*) and edge (*bottom*) of the globule, from the "single-dish" data.

11. Rieko Momose (University of Tokyo)

Barred spiral galaxies have tendency that star formation activities are suppressed in the bar and active in the outer spiral arms(Downes et al. 1996, Sheth et al. 2000, 2002). The low star formation efficiency (SFE) in bar is often discussed as due to gas dynamics on bar (Downes et al. 1996) : however the difference of SFE in bar and spiral arms including the gas kinematics have never been discussed based on solid observation (Regan, Sheth & Vogel 1999, Koda & Sofue 2006). In order to figure out this trend, I need high resolution data in wide areas including outer arms to resolve the gas density and velocity structures of the bar and outer spiral arms.

I therefore observed the barred galaxy NGC 4303 from its central bar to the outer spiral arms. NGC 4303 which is prototypical face-on barred galaxy, is the best example for this study, showing clearly intense star formation in the outer arms but not in the inner bar. In addition, Molecular gas is detected at low resolution in both the bar and spiral arms (Koopmann, Kenney & Young. 2001; Helfer et al. 2003; Kuno et al. 2007). I also have CARMA C-configuration data and Nobeyama 45m (NRO45m) single dish data to probe this. I plan to combine C- and D-configuration and NRO45m data.

11.1. Target

Information about NGC 4303 is below.

RA, DEC(J2000)	12h21m54.9s, +4d28m25.1s
velosity	1556.5 km/s (Koda & Sofue et al. 2006 PASJ.58.299)
distance	16.1Mpc (Ferrarese et al. 1996 ApJ,464,568)
linear scale	$1'' = 78.1$pc
diameter	major 6.5, minor 5.8 arcmin
inclination	27 deg
P.A.	–44.5 deg
morphology	SABbc
AGN	Sy2

11.2. Observation

My observation information is below.

bandwidth	62 MHz
frequency	114.67 GHz
mosaic	19 points
line	CO(J=1-0)

11.3. Results

I made D-configuration map using MIRIAD and combined C- and D-configuration data. (Figures 23, 24, 25)

11.4. Future work

- Combine C- D-configuration data and NRO45m data
- Compare observation result to model

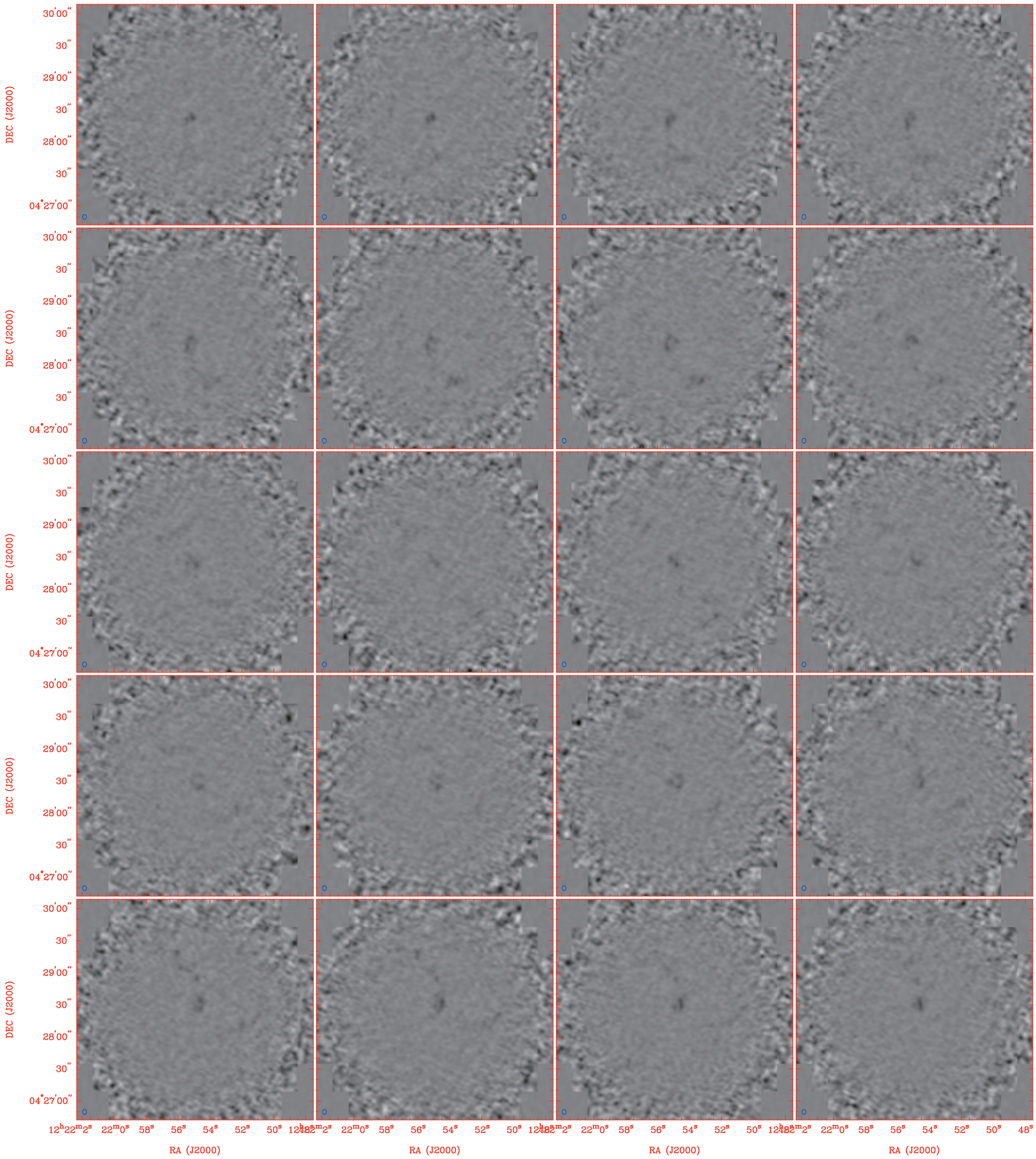

Fig. 23.— Channel map of D-configuration data of NGC 4303.

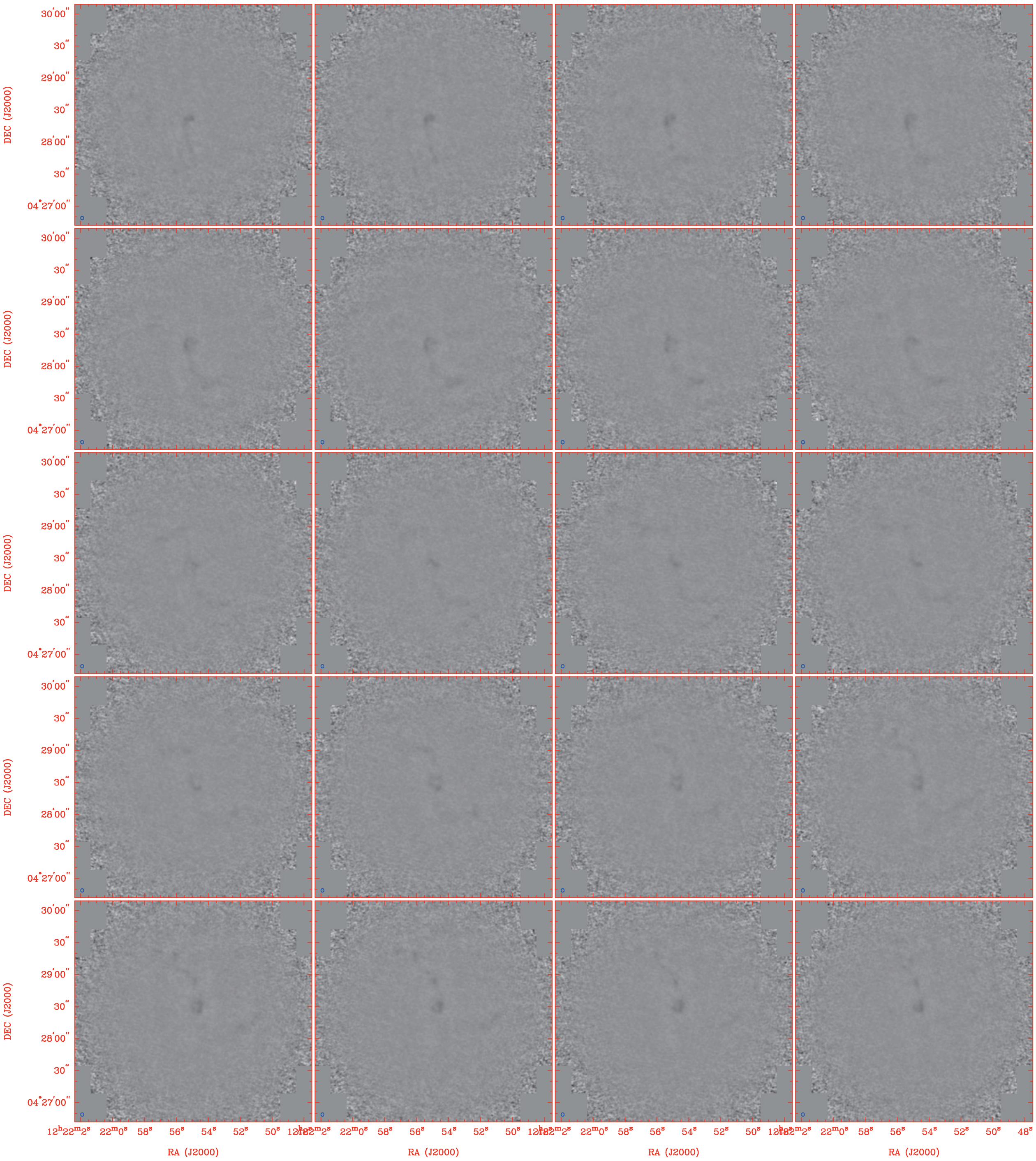

Fig. 24.— Channel map of C- and D-configuration data of NGC 4303.

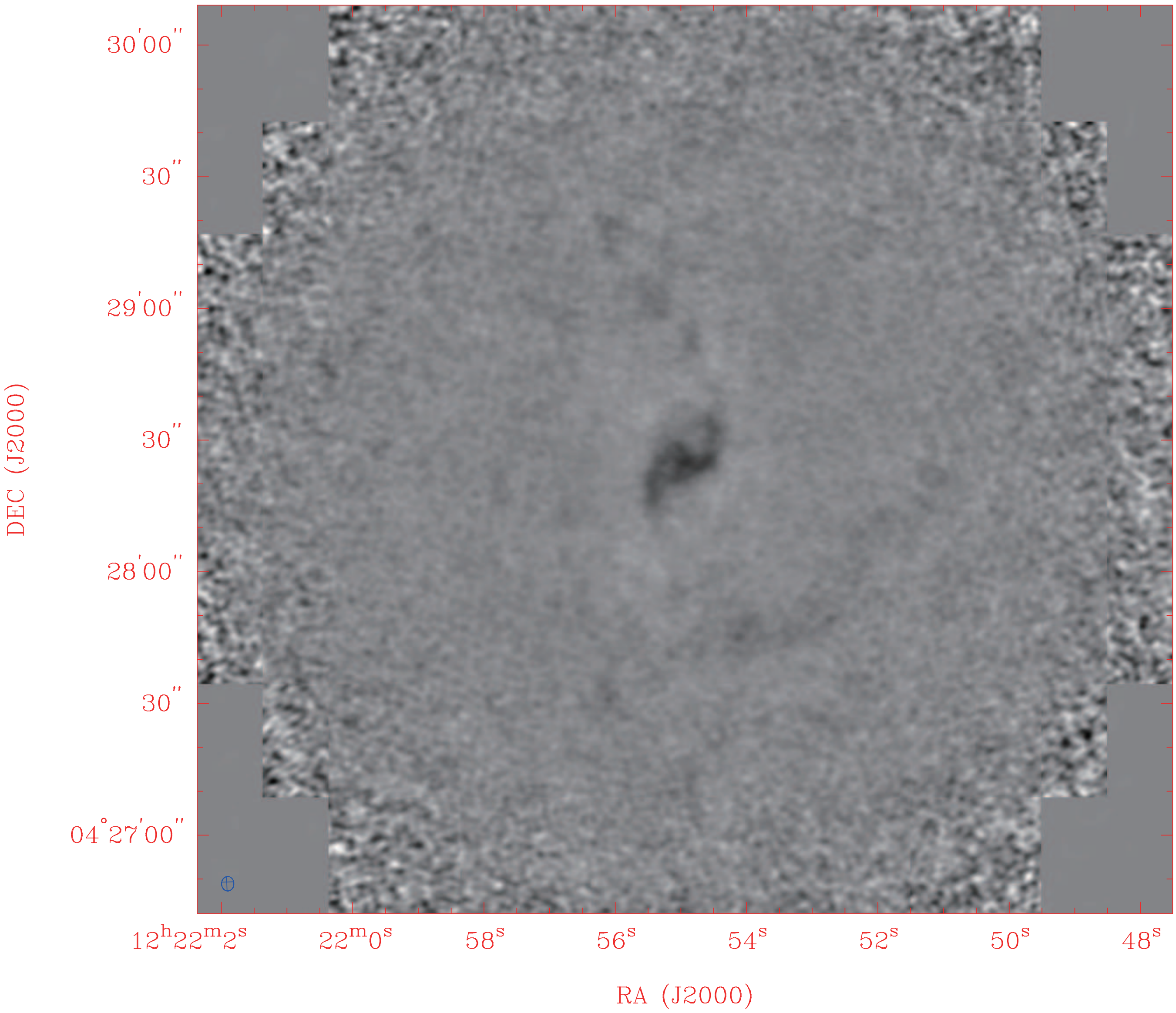

Fig. 25.— Integrated intensity map of C- and D-configuration data. I can detect emission in outer spiral arms.

12. Katherine I.J. Lee (UIUC)

Massive star formation has dramatic impacts on interstellar medium and the sequential star formation (including low mass and massive star formation), and we are interested in understanding massive star formations mechanism. We approach massive star formation by studying the early stage of protostars, since the surrounding environment of the protostars has not destroyed by the stellar wind or the strong ionizing power of massive stars. I05345+3157 is a protocluster with numerous of massive prestellar cores, and thus provides us a region to study early stage of protostars. We propose to observe CS(2-1) line, for CS line provides a tool to trace dense gas. Spitzer telescope has observed this region and observed two dust clumps near I05345+3157 (Klein et al., 2005). Therefore, we can compare CS emission result with dust emission to approach the star formation machenism in star formation region I05345+3157.

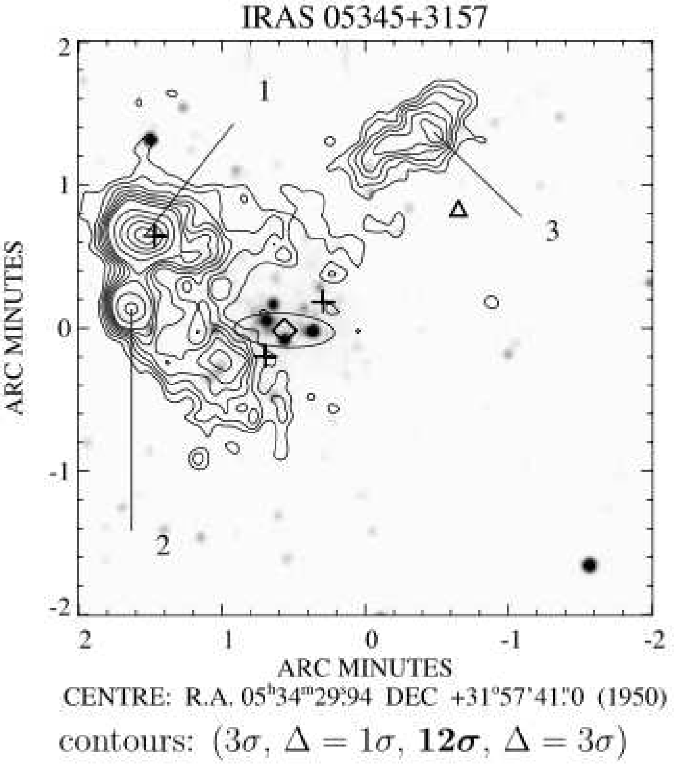

Fig. 26.— Klein et al., 2005 dust observations of I05345+3157.

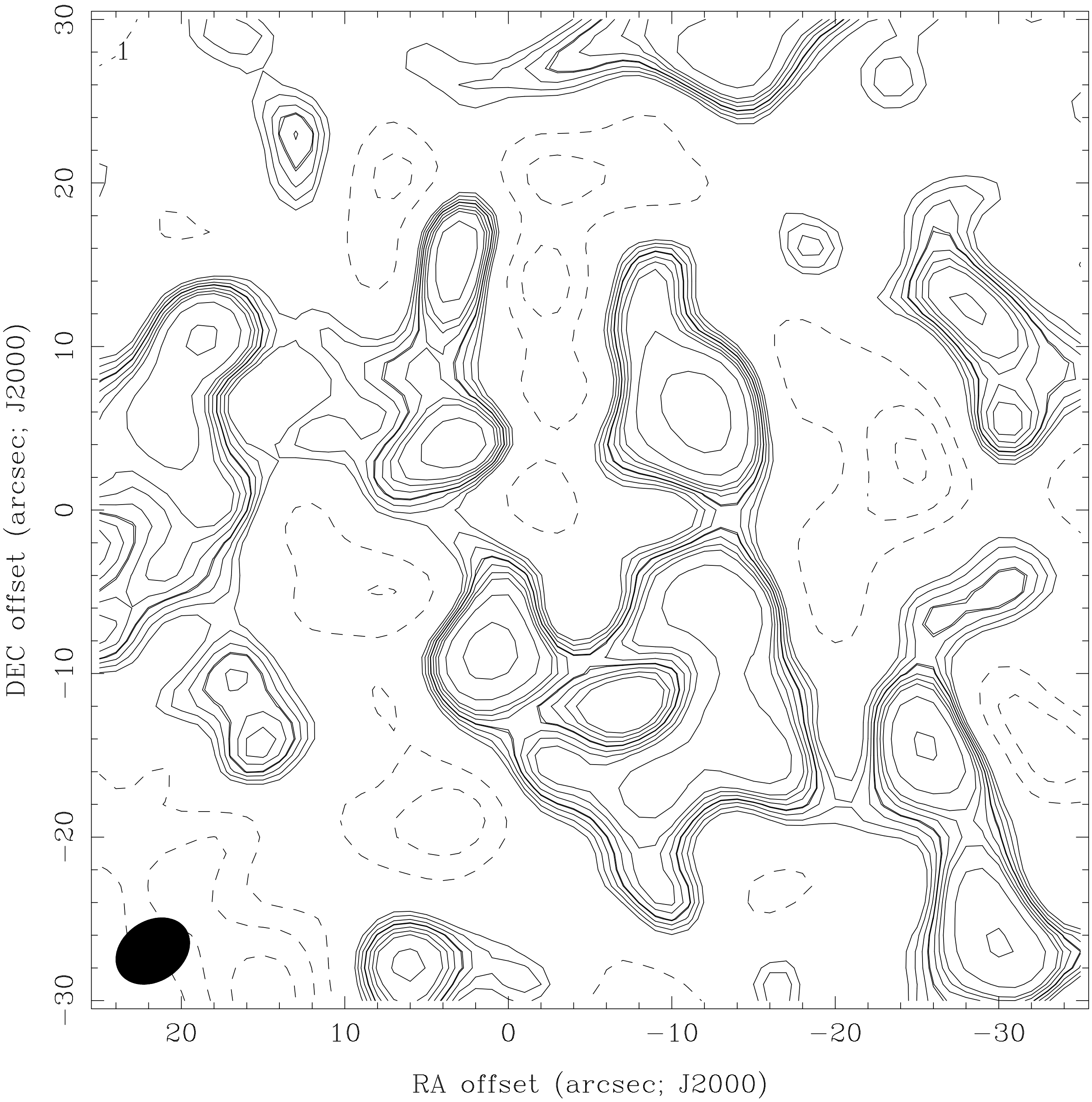

Fig. 27.— CARMA CS(2-1) moment map of I05345+3157.

13. Álvaro Sánchez-Monge (University of Barcelona)

Testing the NH_3/N_2H^+ratio as a chemical clock during the 2008 CARMA Summer School

13.1. Introduction

Very young massive stars are usually surrounded by multiple dense cores, with these cores already forming young stellar objects (YSOs), or with no stellar activity associated (e. g., Beuther et al. 2005; Urquhart et al. 2007). The nitrogenous compounds ammonia (NH_3) and diazenylium (N_2H^+) are excellent tracers to study possible differences in these cores since nitrogen-bearing species do not deplete onto dust grains until densities up to 10^6 cm^{-3} (contrary to carbon-bearing species, such as CO and CS, which deplete at around 10^4 cm^{-3}). Thus, the main differences between NH_3 and N_2H^+ (once the opacity and excitation effects have been taken into account through the treatment of their hyperfine structure) must arise because the cores formed at different times and/or with different initial conditions.

Only very few observational studies, toward low-mass star-forming regions (SFRs), have focused on the comparison of NH_3 and N_2H^+ cores, finding that the NH_3/N_2H^+ ratio is around 60–90 close to the YSOs, while it rises up to 140–190 in starless cores (Caselli et al. 2002; Hotzel et al. 2004). We are carrying out a project to study this ratio toward massive SFRs (Palau et al. 2007; Busquet et al. in prep.), where multiple dense cores in different evolutionary stages are usually found surrounding the massive star. Thus, these regions are excellent laboratories to test the NH_3/N_2H^+ ratio as a chemical clock. Here, I present preliminary results of the N_2H^+(1–0) observations carried out toward the massive star-forming region IRAS 22134+5834 during the 2008 CARMA Summer School. IRAS 22134+5834, with a bolometric luminosity of 12600 $L_\odot$ and located at 2.6 kpc of distance, harbours an hypercompact (HC) HII region located within a cluster of dense cores detected in NH_3 with the VLA.

13.2. Observations

These CARMA observations were obtained on 2008 June 23 in the D-configuration with 14 antennas (five 10.4 m antennas and nine 6 m antennas). The 230 GHz zenith opacity ranged from $\sim$ 0.35 to 0.45 during the observations. The total on-source time was 3.5 hr. The receivers were tuned to an LO frequency of 93.176 GHz, with two overlapping units of 8 MHz centered at 93.174 and 93.181 GHz(LSB) to cover the hyperfine structure of the N_2H^+(1–0) emission, and two 500 MHz units to map the continuum emission at 3 mm. The phase center was α(J2000.0) $= 22^h15^m09\overset{s}{.}23$, δ(J2000.0) $= +58°49'08\overset{''}{.}90$. The gain, bandpass, and flux calibrators were BLLAC, 3C454.3 and MWC349, respectively. Data reduction was performed using the MIRIAD package, and the image was constructed using natural weighting. For the continuum map the synthesized beam is $4\overset{''}{.}90 \times 3\overset{''}{.}68$, with P.A. $= -84\overset{\circ}{.}1$, and the rms noise level is 1 mJy beam^{-1}, while for the N_2H^+ map the synthesized beam is $5\overset{''}{.}32 \times 4\overset{''}{.}05$, with P.A. $= -80\overset{\circ}{.}2$, and the rms noise level is 0.111 Jy beam^{-1}.

13.3. Results

Emission at 3 mm shows a compact single source associated with the HCHII region (see Fig. 28). This source has coordinates $\alpha(\mathrm{J2000.0}) = 22^{\mathrm{h}}15^{\mathrm{m}}09\overset{\mathrm{s}}{.}21$, $\delta(\mathrm{J2000.0}) = +58^{\circ}49'08\overset{''}{.}54$, a peak intensity of 7.2 ± 0.8 mJy beam^{-1}, a flux density of 22.2 mJy, and a deconvolved size of $6\overset{''}{.}8 \times 5\overset{''}{.}4$ with P.A. $= 47^{\circ}$. Assuming a dust temperature of 30 K, a dust emissivity index of 1.5, and a dust mass opacity coefficient of 0.9 cm^2 g^{-1} at 1.2 mm (Beckwith et al. 1990), the dust and gas mass from the 3 mm emission is 26 $M_{\odot}$.

The N_2H^+ emission strongly resembles the NH_3 emission, and a one-to-one correspondence can be made between the NH_3 and N_2H^+ cores. The only exception is the NH_3 core associated with the HCHII region, for which no N_2H^+ emission is detected (see Fig. 28 bottom). Note that both, the NH_3 and N_2H^+ emission, are uncorrelated with the infrared emission (2MASS image in Fig. 28 top), suggesting that these condensations are cold dense cores. In Fig. 29 we show the hyperfine spectrum of the N_2H^+(1–0) transition for the four main cores. Although no millimeter emission is detected toward the dense cores (with a mass sensitivity of 5.9 $M_{\odot}$, a better sensitivity would be necessary) these cores could still be harbouring YSOs. To study this possibility, a high-angular resolution study of molecular outflow emission would help to elucidate the stellar or starless nature of the cores, allowing us to better understand the NH_3/N_2H^+ ratio behaviour. By comparing the NH_3 and N_2H^+ emission in the dense cores we find some differences (see Table 1). Cores C and D have strong NH_3 emission and weak N_2H^+ emission, suggestive of a high NH_3/N_2H^+ ratio, while core A has weak NH_3 emission and strong N_2H^+ emission, suggestive of a low NH_3/N_2H^+ ratio, indicating that core A could be older than cores C and D. Finally, regarding the HCHII region, one would expect a low NH_3/N_2H^+ ratio because there is a YSO already formed. However, we observe the highest value of the ratio, suggesting that the YSO is so evolved and/or massive than temperature and/or ultraviolet radiation effects are destroying N_2H^+ in a more efficient way than NH_3.

Therefore, these N_2H^+ observations carried out with CARMA toward IRAS 22134+5834 allow us to study, together with NH_3 observations, the chemical and physical properties of the multiple cores forming around an HCHII region, and to make a first guess of the evolutionary stage of each dense core in the region.

Table 1: Peak intensity of NH_3 and N_2H^+ for the four main cores toward IRAS 22134+5834

Core	α(J2000.0) ($^{\mathrm{h\,m\,s}}$)	δ(J2000.0) ($^{\circ\,\prime\,\prime\prime}$)	$I_{\mathrm{v}}^{\mathrm{peak}}$ (NH_3) (Jy beam^{-1} km s^{-1})	$I_{\mathrm{v}}^{\mathrm{peak}}$ (N_2H^+) (Jy beam^{-1} km s^{-1})
A	22 15 10.9	+58 48 55	39.6	1.3
B	22 15 09.2	+58 48 53	25.9	0.6
C	22 15 06.8	+58 48 53	61.1	0.6
D	22 15 05.5	+58 48 58	42.2	0.7

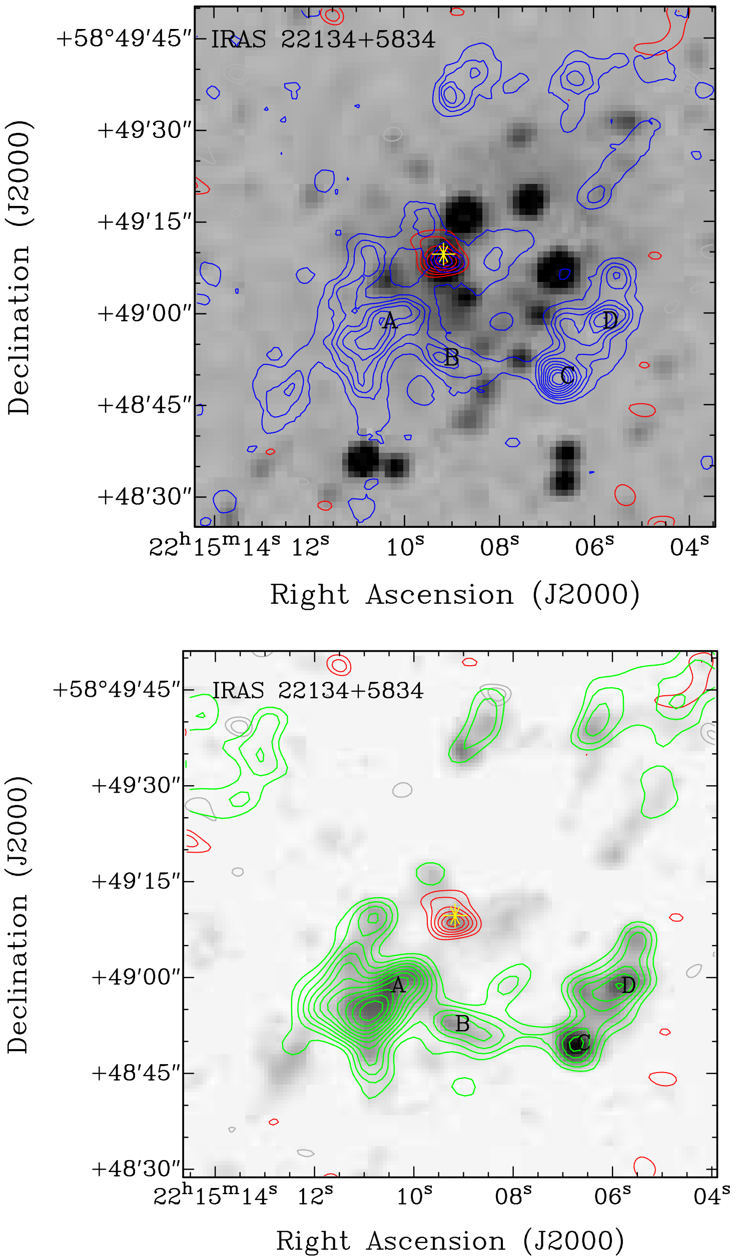

Fig. 28.— IRAS 22134+5834. Top: blue contours: zero-order moment map for the NH_3(1,1) emission observed with the VLA. Contours start at 10%, incresing in steps of 10% of the peak intensity, 61 Jy beam^{-1} km s^{-1}. Red contours: CARMA 3 mm continuum emission. Levels are −4, −3, 3, 4, 5, 6, 7 ,8 ,9 10, and 11 times 1 mJy beam. Grey scale: *K*-band 2MASS image. Bottom: green contours: zero-order moment map for the N_2H^+(1–0) emission mapped with CARMA. Levels are 2, 3, 4, 5, 6, 7, 8, 9, 10, 11, and 12 times 0.1 Jy beam^{-1} km s^{-1}. Red contours: 3 mm continuum emission as in the top panel. Grey scale: zero-order moment map of the NH_3(1,1) emission shown in the top panel. In both panels, the yellow cross indicates the position of the HCHII region, and the A, B, C, and D labels indicate the positions of the spectrum maps shown in Fig. 29.

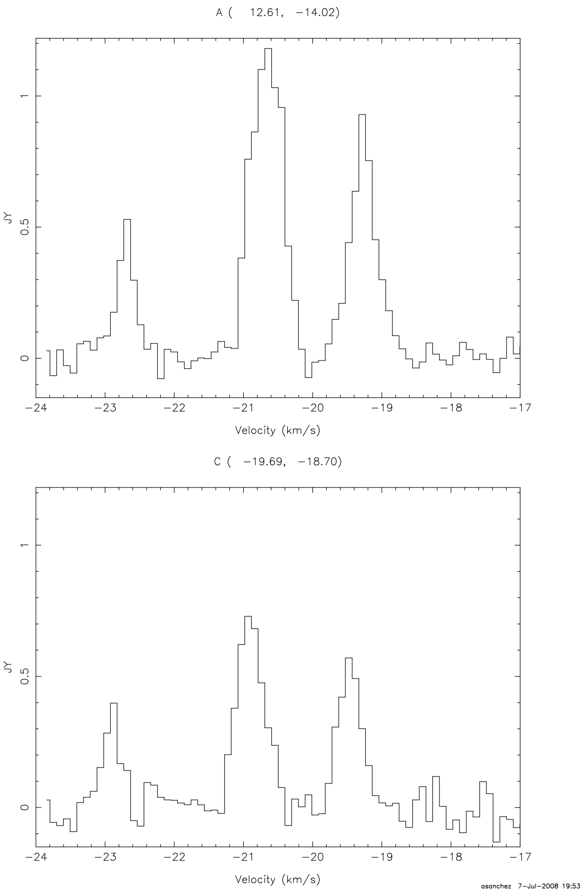

Fig. 29.— IRAS 22134+5834. Spectrum of the N_2H^+(1–0) emission toward the four core peaks (A, B, C, and D) indicated in Fig. 28.

14. Josep-Maria Masqué (University of Barcelona)

A kinematic study of the supersonically contracting star forming core ahead of HH 80N using a non-depleted molecular tracer

14.1. Background

HH 80N is the optically obscured northern counterpart of the brightest Herbig-Haro objects known, HH 80-81 (Martí et al. 1993), located at 1.7 kpc of distance (Rodríguez et al. 1980). Ahead of HH 80N there is a massive (M $\sim 20\ M_{\odot}$) and large ($\sim$ 0.2 pc in radius) molecular dense clump that shows star forming signatures, namely a bipolar CO outflow and a supersonic infall velocities ($\sim$ 0.6 km s^{-1}) (Girart et al. 1994, 1998, 2001; Masqué et al. 2008). Interestingly, this infall velocity differs significantly from what standard contracting core models predict (e.g. Shu et al. 1987) or what is observed in other contracting cores (Furuya et al. 2006). This rises the question whether the HH 80/81/80N flow has triggered or sped up the star formation process in this core.

The observational study of the infall process has, however, an important drawback: the depletion of the molecules onto dust grain mantles that, at densities higher than 10^5 cm^{-3}, becomes dramatically efficient for a number of species (Aikawa et al. 2001). In fact, the previous studies of the HH 80N core found that the molecular species traces an infalling ring-like structure, that is likely not real but the result of a strong molecular depletion at the inner and denser regions of this core. Consequently, the kinematic information about the central regions of the HH 80N core is missed. In order to surpass this problem, it is necessary to map the core using a molecular tracer that has little or no depletion. During this decade, detailed studies shows that nitrogen bearing molecules are less affected by depletion (Tafalla et al. 2002; Aikawa et al. 2001). In this work I present observations of N_2H^+ towards the HH 80N region. The goal is to characterize the kinematic properties at the center and denser parts of the HH 80N core and to complete the overall kinematic description of this core.

14.2. Observations and Results

The CARMA array observations were carried out on 2008 June 26 in the D-configuration. The phase calibrator was 1911-201 and the flux and bandpass calibrator was MWC349. The 230 GHz zenith opacity ranged from 0.47 to 0.61. The phase tracking center of the observations was set at $\alpha(J2000) = 18^{\rm h}19^{\rm m}18\overset{\rm s}{.}618$ and $\delta(J2000) = -20^{\circ}40'55\overset{''}{.}00$. The correlator was configured in two spectral windows of 2 MHz to cover the isolate hyperfine line N_2H^+ (1–0) F_1 (0–1) and OCS (8-7), plus four other windows of 500 MHz to map the continuum emission. The typical window for the line observation provides an spectral resolution of 32 KHz, which corresponds to a velocity resolution of $\sim$ 0.1 km s^{-1}, ideal to study infall motions.

The left panel of Figure 1 shows the zero order moment map of the N_2H^+ emission superimposed over the 8 μm Spitzer image, retrieved from the Spitzer archive. Note in the 8 μm that the HH 80N core is seen in absorption (black color) and the central peak likely coincides with the protostar that powers the CO outflow. The N_2H^+ emission appears more compact than the elongated structure seen in the Spitzer image, tracing only the south-east part and has the peak displaced eastwards from the 8 μm peak. This suggests that there may be a dense starless clump located eastwards from the central protostar or in a foreground position with respect to the HH 80N core.

The right panels of Figure 1 show the position-velocity plots along the major (upper panel) and minor (lower panel) axis of the elongated HH 80N core. Clearly, the PV plot along the minor axis reveal two velocity components, consistent with the infalling velocity of 0.6 km s^{-1}. On the other hand, the PV plots along the major axis, in spite of having more complexity, shows that N_2H^+ is significantly more compact than other molecular tracers used in previous studies. This indicates that N_2H^+ is probably tracing gas from the inner region of the core depleted in other molecules. However, this preliminar analysis is not conclusive since the kinematics of the most inner regions is still veiled. Probably, the combined observations with the CARMA array at D and C configurations will provide enough sensibility and angular resolution to study the behavior of N_2H^+ at smaller scales.

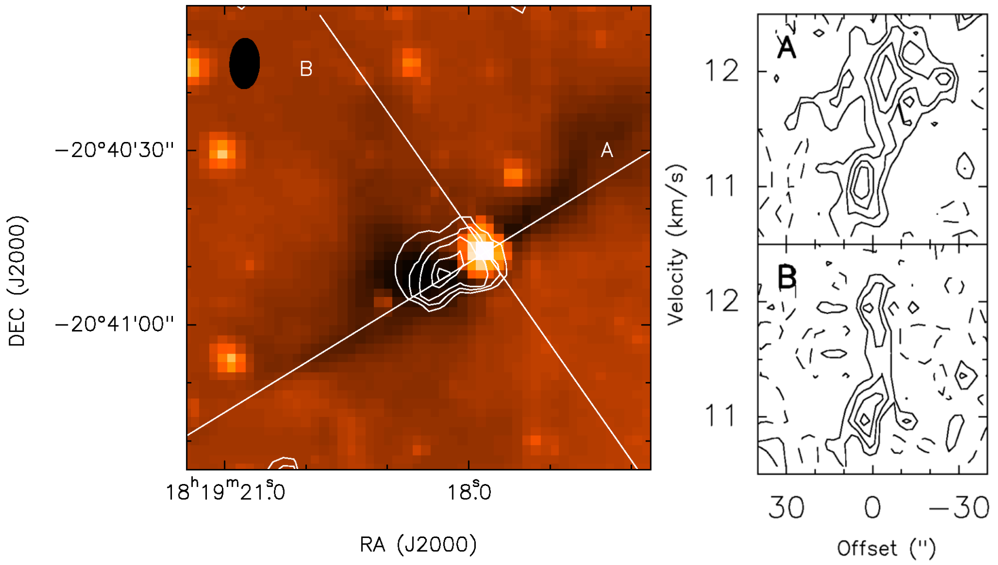

Fig. 30.— Left: Superposition of the Spitzer image (8μm; color scale) and the zero-order moment (integrated emission; white contours) over the $\sim$ 10.5–12.5 km s^{-1} velocity range. The beam is shown at in the upper left corner. The solid lines represent the major (A) and minor (B) axis of the core. Right: Position-velocity plots along the major and minor axis of the core.

15. Lei Zhu (CfA)

15.1. Background

The original idea of my project is to study the infall activity at the early stages of massive star formation. I chose W3-SE as my target, a molecular dense core without 6 cm emission (Tieftrunk et al. 1998) and IRAS point sources (Jijina et al. 1999). However, there is an IR jet explained as 2μmH_2 vibration emission (Tieftrunk et al. 1998). Its driving source should be embedded deeply in the W3-SE core, indicating ongoing star formation activity. Recently, Wu et al. (2007) observed W3-SE using IRAM 30-m with multiple molecular lines. Compared with the optically thin lines such as N_2H^+(1-0) and $C^{18}O$(1-0), the line profiles of HCO^+ (1-0) and (3-2) showed a typical infall signature (see Fig.1). However, the angular resolution of the single-dish observation cannot exclude the effects of multiple cores or outflow.

15.2. Goals

To investigate the details of W3-SE with high resolution. (1) to observe HCO^+(1-0) line to confirm/reject the infall and to study the roles of the possible infall and outflow at the early stages of massive star formation; (2) to observe the 3-mm continuum to determine the mass distribution, multiplicity and dust properties (along with sub-mm continuum data from the JCMT).

15.3. Observation

The observation was carried out with the CARMA in the D-configuration at 3-mm wavelength, which achieved a beamsize of about 6$''$. It included two tracks. The first one on June 24th lasted for 5 hours with 19-point mosaics, and the second one on June 27 lasted for 4 hours with 7-point mosaics. The first track was on the maintenance day, and a portion of about 15% of the uv data was flagged in the following reduction. Finally, I merged the two data sets for analysis. The correlator configuration was two 500-MHz bands for the 3-mm continuum, two LSB narrow bands (one 8 MHz and one 32 MHz) for the SiO (2-1) at 86.2 GHz, and the two corresponded USB narrow bands for HCO^+ (1-0) at 89.2 GHz. The highest velocity resolution is 0.42 km s^{-1}.

15.4. Results

15.5. 3-mm Continuum

The weak 3-mm continuum of W3-SE is shown in Fig.2. The morphology includes an un-resolved core plus weak extention in the east direction. The Gaussian fitting gives a total flux of 55$\pm$10 mJy beam^{-1}. Alternatively, the sum of the pixels ($> 3\ \sigma$) in this region gives a total flux of 73 mJy. On the other hand, with the JCMT data I have measured a total flux of 111.25 Jy in the same region at 450 μm and 13.39 Jy at 850 μm. Therefore, the spectral indexes are 3.8 between 450 μm/3 mm, and 4.0 between 850 μm/3 mm. The results roughly agree with the spectral index of 3.3 between 450/850 μm. The large spectral index ($\sim$4) is also consistent with the absence of 6 cm continuum (Tieftrunk et al. 1998), indicating the donmination of dust thermal emission at 3-mm wavelength.

15.6. HCO^+(1-0)

The HCO^+(1-0) emission in W3-SE is very bright. Fig.3. presents the HCO^+(1-0) integrated intensity map. The intensity peak (marked as A) is consistent with the 3-mm continuum peak. The total flux of the whole region is 135 Jy km s^{-1}. Compared with the 3-mm continuum map, the HCO^+(1-0) integrated intensity map provides more details, including the extension in the north and southeast directions, as well as a halo enveloping the whole region.

Fig.3 also shows the spectra from the central core and the the northern (position B) and southeastern (position C) extensions. The spectra at positions A and B present double peaks and line wings, while the spectrum at position C have only one peak and nearly no wings. In addition, at positions A and B, the profiles of the two velocity components are asymmetric, i.e. the inner edges of them are sharper than the outer edges. This feature, along with the peak velocity of the optically thin lines from single-dish observation, strongly indicates the self-absorption of HCO^+ instead of two independent cores with different velocities.

The channel maps of HCO^+(1-0) is presented in Fig.4. The velocity range of the blue component is from -38.6 to -45.1 km s^{-1}, and the one for the red component is from -32.4 to -37.7 km s^{-1}. I made the integrated intensity map for the two components, showing in Fig.5.a. Besides, noticing the wings of the two components, I also made the integrated intensity maps for them (from -42.3 to -45.1 km s^{-1} for the blue wing and from -32.4 to -34.9 km s^{-1} for the red wing), shown in Fig.5.b. Both the blue and red components, as well as the blue and red wings, show the northern extension, although with some small displacements. The detailed analysis and modeling are ongoing.

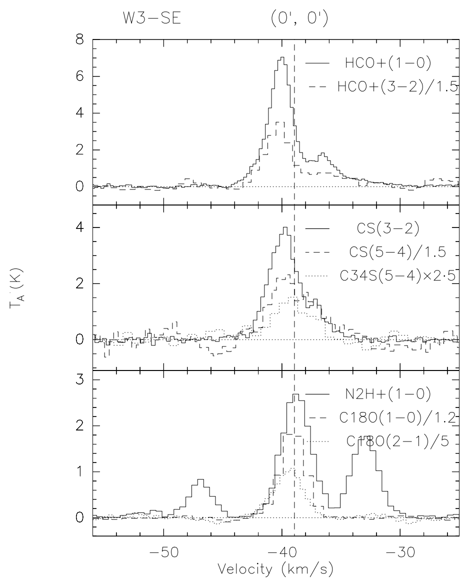

Fig. 31.— The single-dish spectra from IRAM 30-m. There seems to be a red-shifted self-absorption feature in the HCO^+(1-0) and (3-2) line profiles. The velocity of this feature is consistent with the peaks of optically thin line N_2H^+(1-0) and $C^{18}O$(1-0) and (2-1).

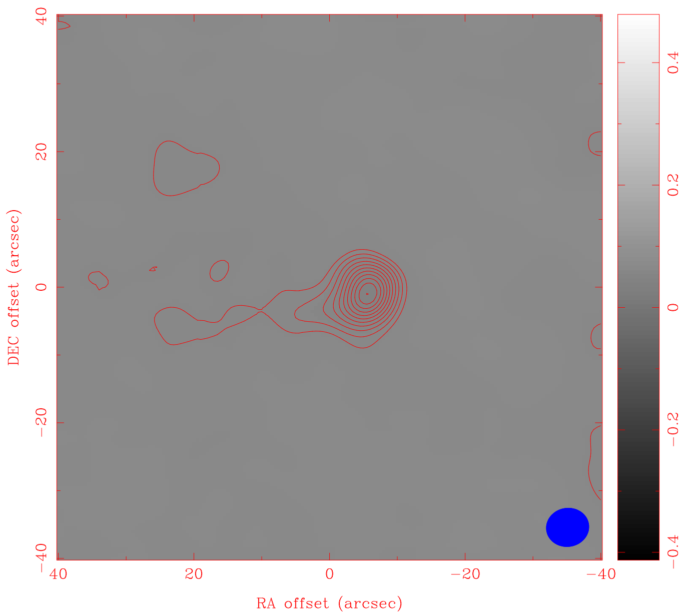

Fig. 32.— The 3-mm continuum image, obtained from the combination of two 500 MHz bands. Contours are 2n σ, n=2, 3, 4, ... The value of 1 σ is 1 mJy beam^{-1}. The beam size is $6.24'' \times 5.62''$.

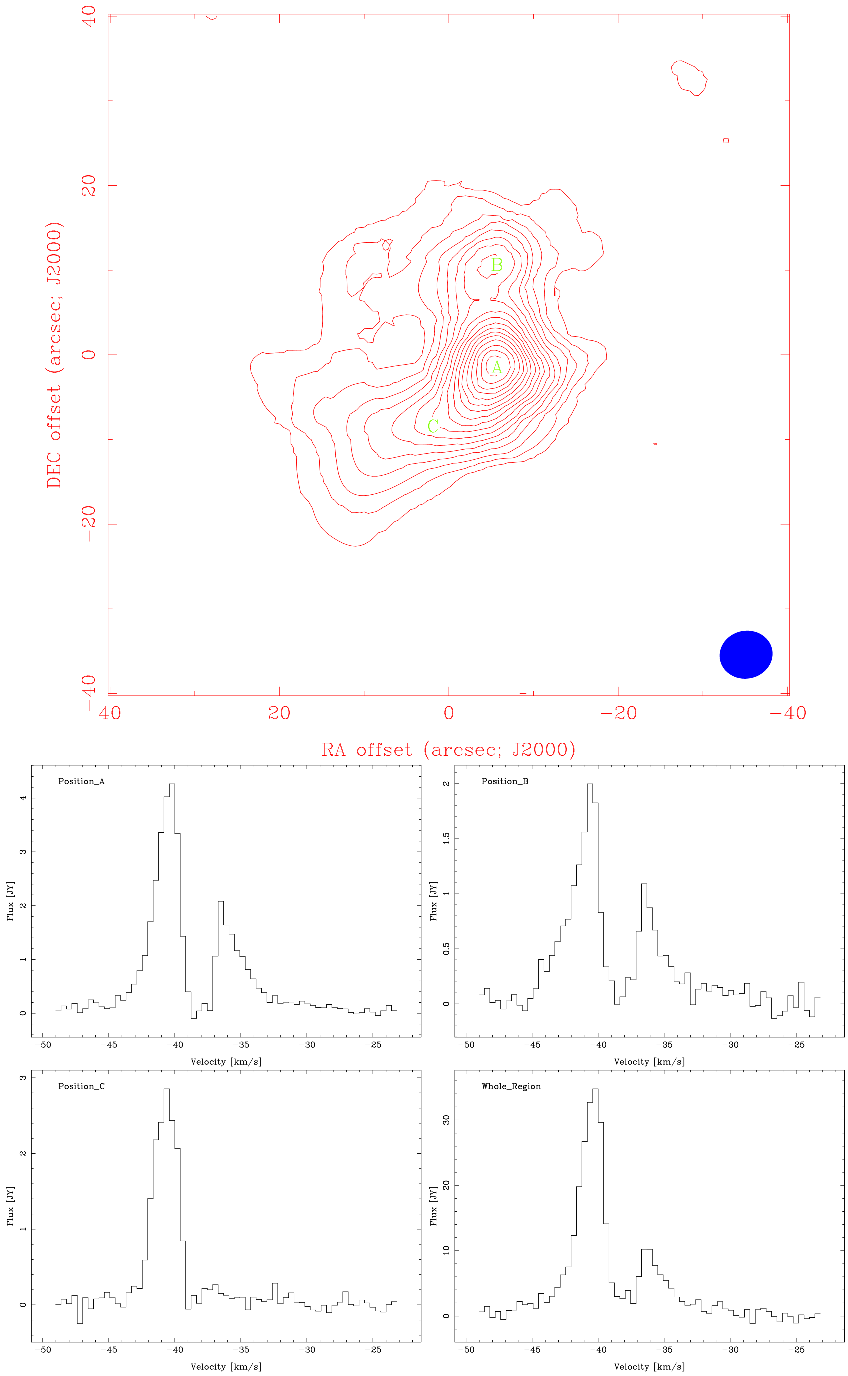

Fig. 33.— The integrated intensity map of HCO^+(1-0) and the spectra. For the integrated intensity map, the contours are 4 and 40n σ, n=1, 2, 3, 4... The value of 1 σ is 20 mJy beam^{-1} km s^{-1}. The beam size is $6.28'' \times 5.65''$. The first three spectra are from the position A, B and C, which are marked in the integrated intensity map, and the forth spectrum is from the integration over the whole region.

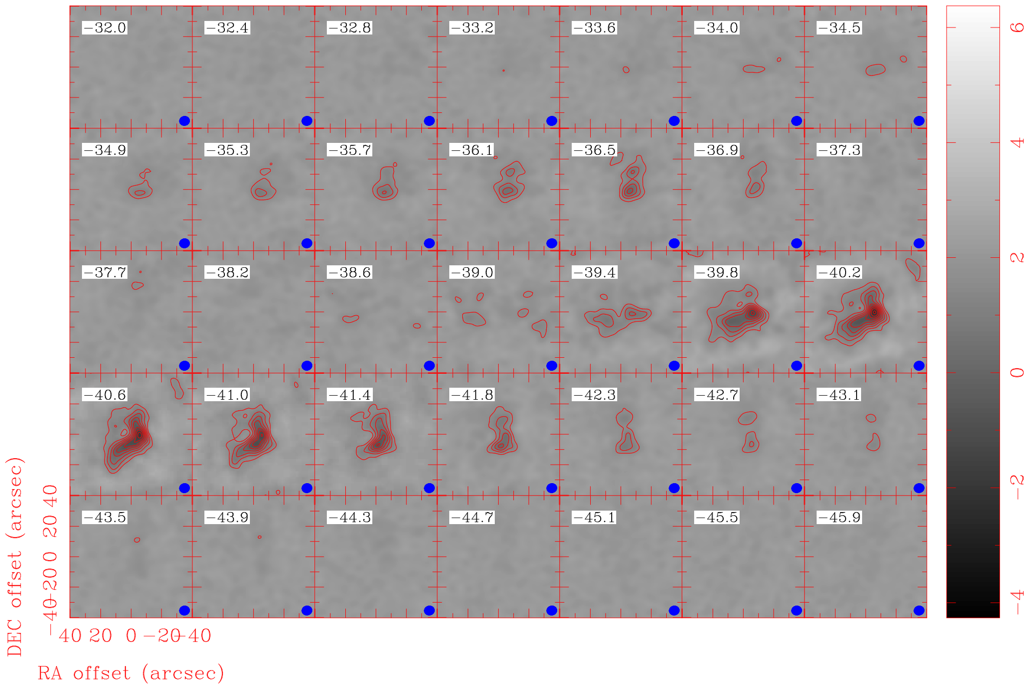

Fig. 34.— The channel map of the HCO$^+$(1-0). The width for each channel is about 0.4 km s^{-1}. The contours are 4n σ, and 1 σ equals to 120 mJy beam^{-1}.

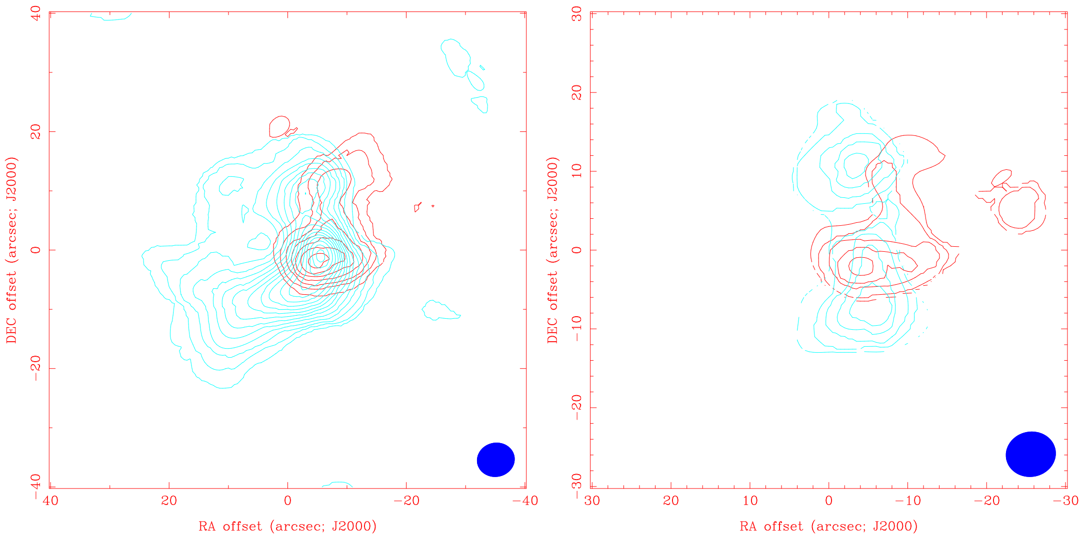

Fig. 35.— The integrated intensity map for the blue and red components. Contours are 4 and 20n σ, n=1, 2, 3, 4... The value of 1 σ is 30 mJy beam^{-1} km s^{-1}. The integrated intensity maps for the (*left*) blue-wing and (*right*) red-wing. In the map for the blue wing, contours are 4n σ, n=1, 2, 4, 6, 8. The value of 1 σ is 40 mJy beam^{-1} km s^{-1}. In the map for the red wing, contours are 4n σ, n=1, 2, 3, 4. The value of 1 σ is 60 mJy beam^{-1} km s^{-1}

16. Masayuki Fukuhara (University of Tokyo/Nobeyama Radio Observatory)

The GMA Evolution Across the Western Spiral arm in M83

The evolution of interstellar medium (ISM) is strongly influenced by large-scale galactic dynamics (e.g. galactic shock, shear). Among ISM, giant molecular cloud associations (GMAs) are the most massive $\sim 10^7 M_\odot$, and hosting virtually all high-mass star formation. Thus, the evolution of GMAs have a critical importance to understand the mechanism of star formation. Although edge-on Galaxy has an uncertainness about GMAs position, relation between GMA evolution and galactic structure (e.g spiral arm, bar) should be investigated by the observation of face-on extra galaxies. Since detail studies of GMA evolution are difficult due to limited sensitivity and angular resolution, GMA formation and destruction are poorly understood by observation.

In order to understand GMA properties and star formation in arms and inter-arms, we have been observing M83 using interferometer and single dish telescope. M83 is one of the best targets to investigate ISM evolution across spiral arms because it is nearby(4.5Mpc), face-on, grand-desig spiral galaxy. Although the declination of M83 is low, we can get good synthesized beam pattern of interferometer if we observe using many array configurations or using interferometer such as CARMA which has many baselines. Other way round, M83 will be observed using ALMA to investigate full details of ISM evolution since good observing condition of M83 at ALMA site. It is significant to study ISM evolution of M83 before ALMA operation will be started.

Last year, we carried out three points mosaicing observations across the western spiral arm of M83 in the CO(J=1-0) using Nobeyama Millimeter Array (NMA). Since missing flux is critical problem for GMA evolution, we combined NMA data with Nobeyama 45m telescope (NRO45m) data and identified 19 GMAs on the arm and 7 GMAs on the upstream inter-arm and 5 GMAs on the downstream inter-arm (see Figure 36). But some GMAs on the inter-arm are extended out of primary beams and we could not search the properties such as size, mass and star formation rate of them. In this year, we carried out four points mosaicing observations using NMA around last year observation fields to identify more GMAs on the inter-arms and search the properties of them. Although we obtaind high resolution data of NMA, soon after the changging configuration to the most compact array, 2 antennas of NMA were broken and not available. Therefore, we could not obtain enough data of compact array configuration using NMA at these four points mosaicing fields.

In order to fill the gap between high resolution data of NMA and NRO45m data in Fourier space, we carried out four points mosaicing observation in the CO(J=1-0) using D array configuration of CARMA in my student project of CARMA summer school 2008. The CARMA consisted of six 10m antennas and ten 6m antennas which provide primary beams of about $60''$ and $100''$ at 115GHz respectively, but two 10m antenna were not available at our observation. Observational date was 26 June 2008 and the system noise temperatures were 900 K at SSB. The back end were two narrow band correlators (band width 31MHz) which have enough high velocity resolution to be combined with NMA data, and one wide band correlator (band width 500Mhz). Four pointings were observed by turns to get uniform $u-v$ coverage for each observation field. The quasar 1337-129 was used for both gain calibrator and bandpass calibrator. The flux scale of the maps was determined through observations of Mars.

The raw visibility data of CARMA were calibrated with the program package MIRIAD. The calibrated visibility data were Fourier-transformed using MIRIAD task INVERT setting natural weight, and map were cleaned using MIRIAD task MOSSDI. The deconvolution of all the pointings was done together and applied primary beam correction. The final map had an angular resolution of $9.6'' \times 4.4'' (\sim 210\mathrm{pc} \times 100\mathrm{pc})$, a velocity resolution of 2.6km/s (1MHz) same as that of NMA data qnd a typical noise level was about 200 mJy/beam. Figures 37 and 38 show an velocity integration intensity map and a velocity channel map. The velocity structure of arm are consistent to NMA data. After this CARMA summer school, we will combined this CARMA data with NMA and NRO45m to obtain the highest-fidelity large CO map. Thank you.

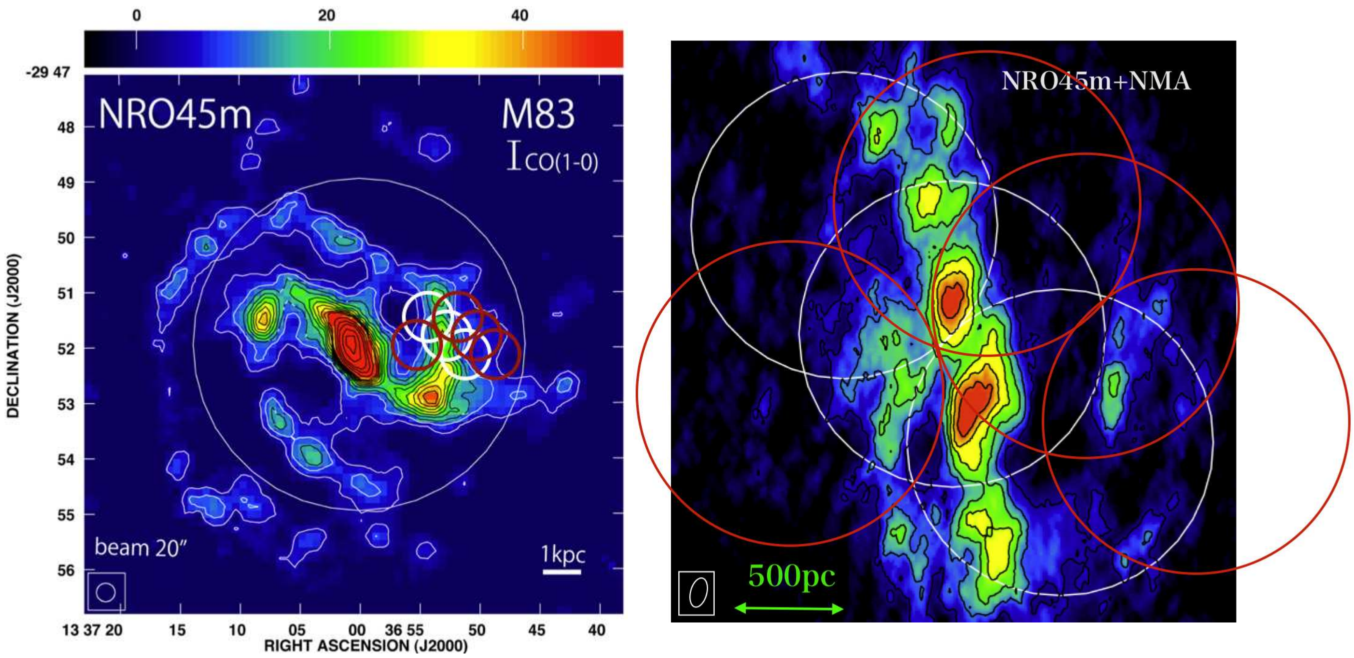

Fig. 36.— A contour map of the CO(1-0) velocity integration intensity map using NRO45m (left) and the NMA+NRO45m combined map (right). Three white circles represent the F.O.V.s of the old NMA observation, and four red circles represent the F.O.V.s of new NMA observation and CARMA observation.

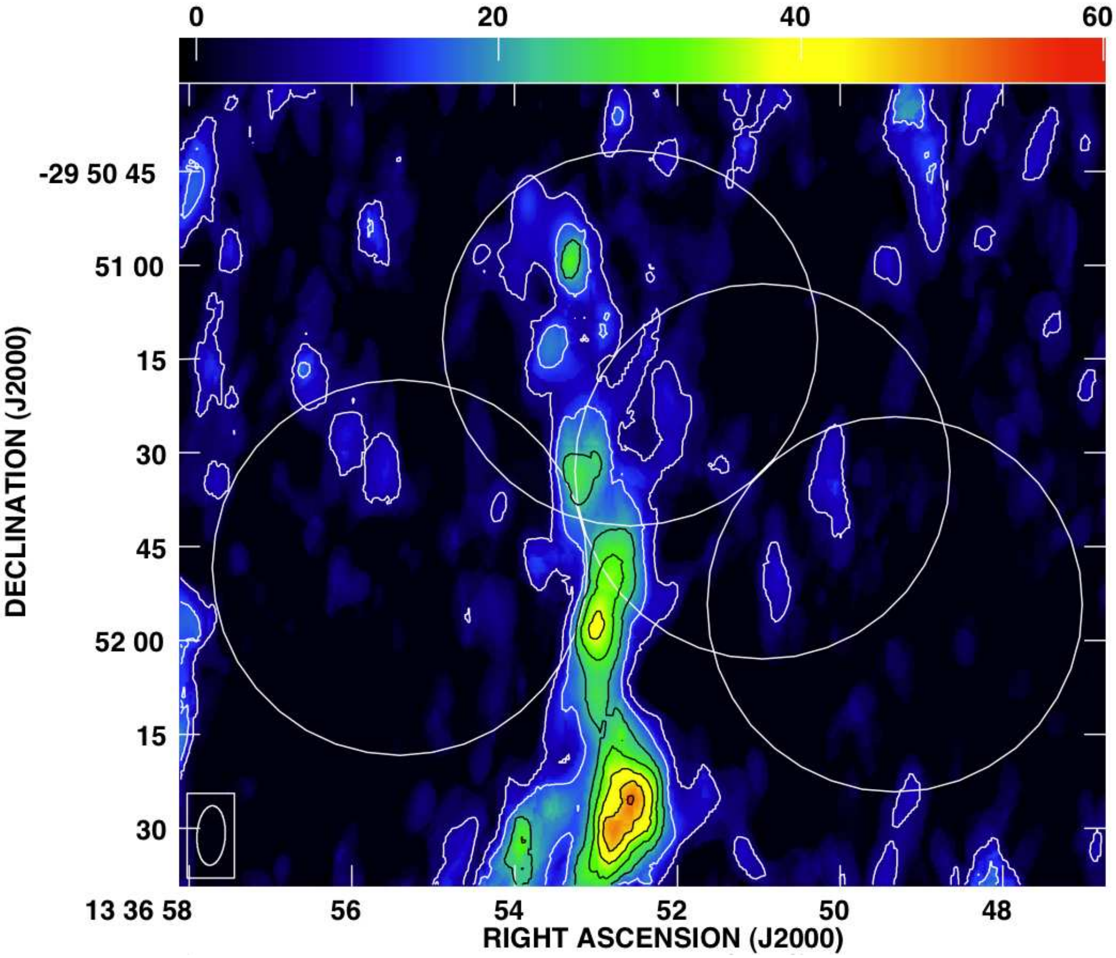

Fig. 37.— A contour map of the CO(1-0) velocity integration intensity map using CARMA. Four white circles represent the F.O.V.s of CARMA observation. The contour interval and lowest contour of the velocity integration intensity map are 7.5 Jy/beam km/s.

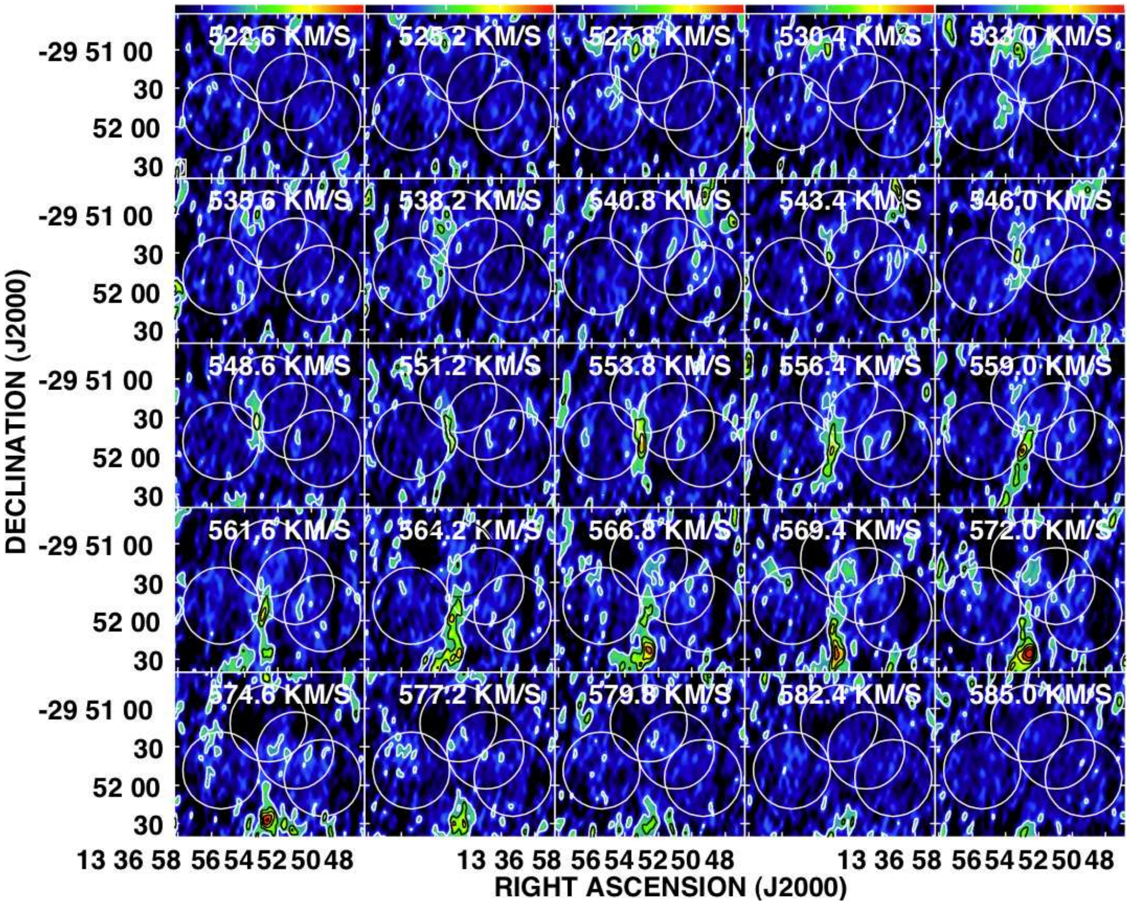

Fig. 38.— A velocity channel map of the CO(1-0) using CARMA. Four white circles represent the F.O.V.s of CARMA observation. The contour interval lowest contour of the channel map are 3σ

17. Amanda Heiderman (University of Texas) and Joe Converse (Berkeley)

Galaxy tidal interactions and mergers of gas-rich galaxies show an increase in the star formation rate (SFR) on average compared to isolated field galaxies. During the interaction, shocks and gravitational torques that drive the gas inwards leading to supercritical gas densities and an enhancement in the SFR. We observe an interacting luminous infrared galaxy NGC 6090 in CO (1-0) using CARMA, which has an extensive set of multi-wavelength observations including, HST WPC and NICMOS, and Spitzer IRAC, MIPS, and CO (1-0) from NRAO 12m. With these data and the addition of the CARMA CO map, we attempt to resolve regions of dense gas fueling the star formation and compare this to other SF tracers in this interacting pair.

The results from our CARMA observations are shown in Figures 39 and 40. We detected emission in 4 channels with a beam size of $5.7'' \times 3.6''$ (Fig 39). The greyscale optical HST ACS F814W image is displayed in Fig 40, showing the extent of the faint tidal tails in this interacting pair. The CARMA CO (1-0) contours (yellow) are overlayed on the HST image (top right) showing the dense gas to be concentrated in the center of the double nuclei. The blue oval on the optical image indicates CARMA beam size.

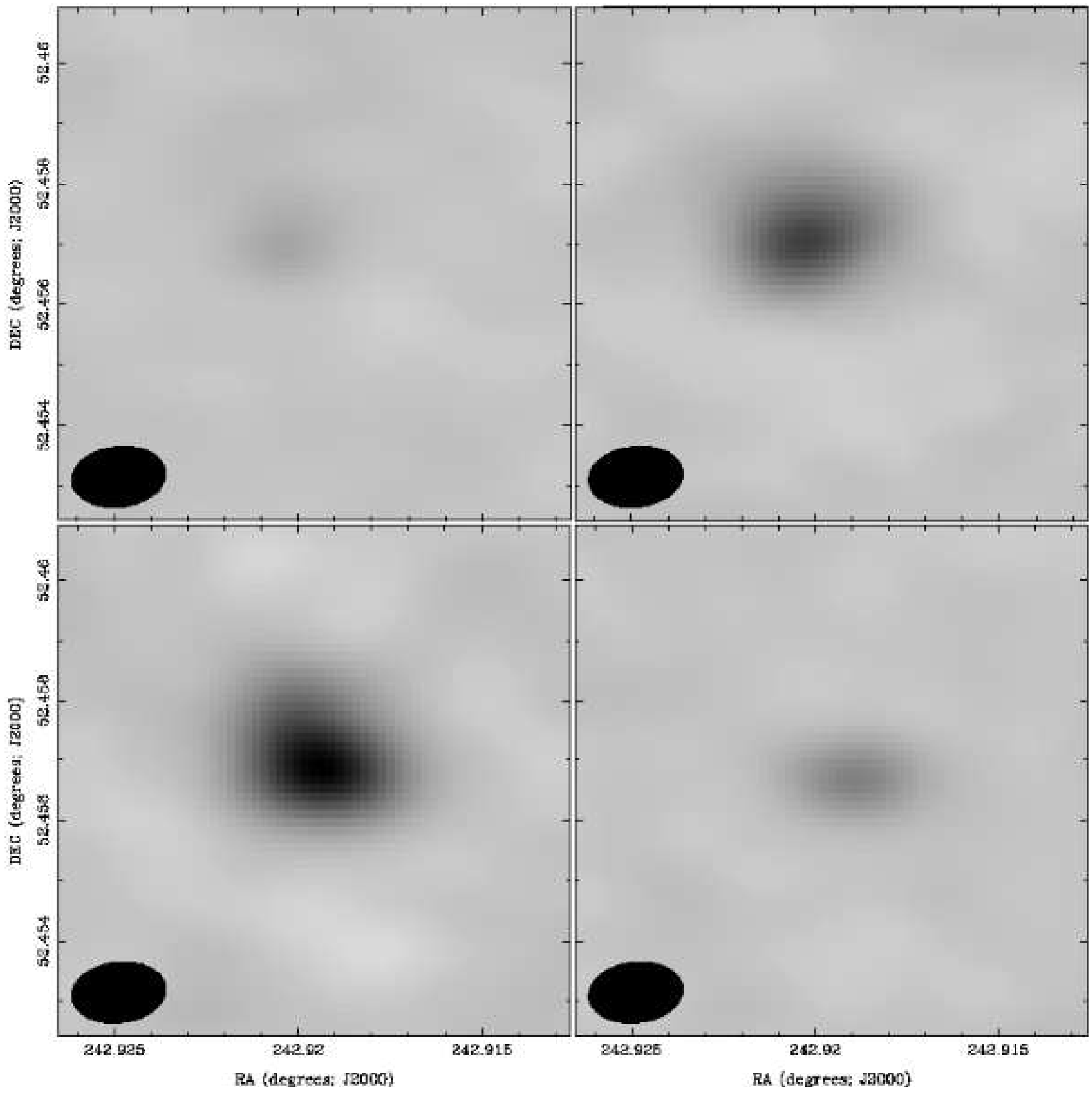

Fig. 39.— CO(1-0) emission from NGC 6090 detected with CARMA.

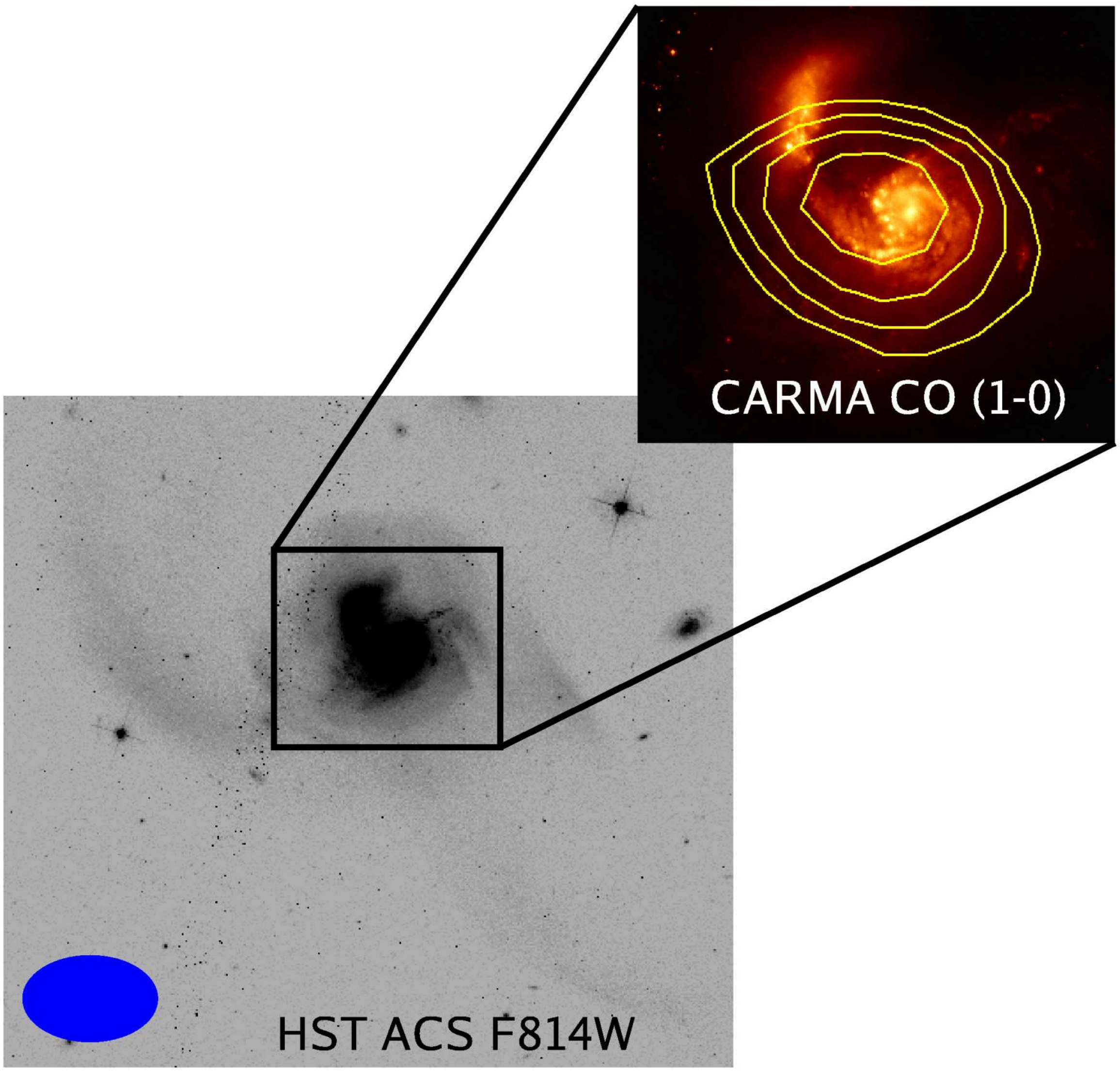

Fig. 40.— HST image of NGC 6090 overlaid with CO contours (yellow).

18. Megan Roscioli (University of Chicago) and Nicole Hasler (University of Alabama, Huntsville)

95 GHz Measurement of quasar 3C186 with CARMA

18.1. Motivation

Galaxy clusters are the largest gravitationally bound structures in the universe. According to hierarchical structure formation theory, galaxy clusters are the most recently formed astrophysical objects. As such, they have formed during an era when dark energy is believed to dominate the matter density of the universe. Although today dark energy is believed to account for approximately 70 % of the matter density, cosmologists know very little about it. Because dark energy causes the universe to accelerate in its expansion, it inhibits the formation of large structures. Thus the number of galaxy clusters formed as a function of cosmic time is a sensitive probe of the mysterious dark energy.

When photons from the cosmic microwave background (CMB) pass through the hot gas in the deep gravitational potential wells of galaxy clusters, some fraction of them interact with the hot gas and gain energy from it. When the CMB is observed at low frequencies, some of the photons are "missing" in the location of the galaxy cluster because they have been boosted to higher energy, causing a decrement at the location of the cluster. This effect is called the Sunyaev Zel'dovich (SZ) effect. Galaxy clusters can be detected by this signature in the CMB. One of the nice features of this detection method is that (unlike X-ray or optical observations) the strength of the SZ signal has little dependence on the redshift of the cluster (). This enables galaxy cluster surveys conducted in SZ to be more complete at high redshifts.

Operating at 30 and 95 GHz, the Sunyaev-Zel'dovich Array (SZA) is designed as a compact array of 6 antennas plus 2 antennas located farther away from the others. The configuration is designed to be most sensitive to cluster-scale objects and to also collect data at higher resolution in order to detect point sources that fill in the SZ decrement of clusters. While the SZA was located in the Owens Valley, it was sometimes difficult to obtain good measurements of point sources at 95 GHz due to phase decoherence from atmospheric instability, which would cause us to underestimate the flux of the point sources. Reliable, high resolution measurements of any central point sources in clusters are important for accurately determining the extent of their SZ signals. Also, from a more educational viewpoint, it is instructive to combine SZA and CARMA data, anticipating the upcoming synthesis of the arrays into a combined array. The highest redshift cluster that has been observed to date in the SZ effect is a cluster at redshift 1.067 (). This cluster contains the quasar 3C186 (RA 07:44:17.45, dec +37:53:17.15). In this project, we have taken advantage of the high angular resolution of CARMA to accurately measure the flux of the point source and subtracted this flux from the SZ decrement of the cluster to obtain a more accurate SZ map of the cluster.

19. Observations

We conducted observations with CARMA on June 26, 2008 as part of the 2008 CARMA summer school. The antennas were positioned in the D-array, with 3-6” resolution at 100 GHz. We observed at 95 GHz, utilizing the full bandwidth of CARMA. The weather was good, typical for the site for 95 GHz observations. We observed for 5 hours, with 20 minutes on source and 2 minutes to observe a phase calibrator for each cycle. We used 0927+390 as a phase calibrator and conducted radio pointing on Mars. We used our phase calibrator to calibrate the bandpass as well. Data were reduced using the MIRIAD software package. We flagged and excluded from the analysis all data taken when the antennas were pointed near zenith and there was some loss of tracking that was not automatically flagged.

20. Results

We observed 3C186 with CARMA (see Figure 41). We measured the flux of this point source to be 5.5421 mJy. Dan Marrone observed the cluster at 3C186 with the SZA at 95 GHz. Using DIFMAP, we subtracted a modeled point source with 5.5421 mJy flux from the center of this cluster. See Figures 42 and 43 for the cluster SZ maps before and after the point source subtraction.

We note that the decrement in the unsubtracted map is not obvious, but that there may be some decrement near the cluster position. However, we can clearly see the SZ decrement of the cluster after the flux from the point source has been subtracted.

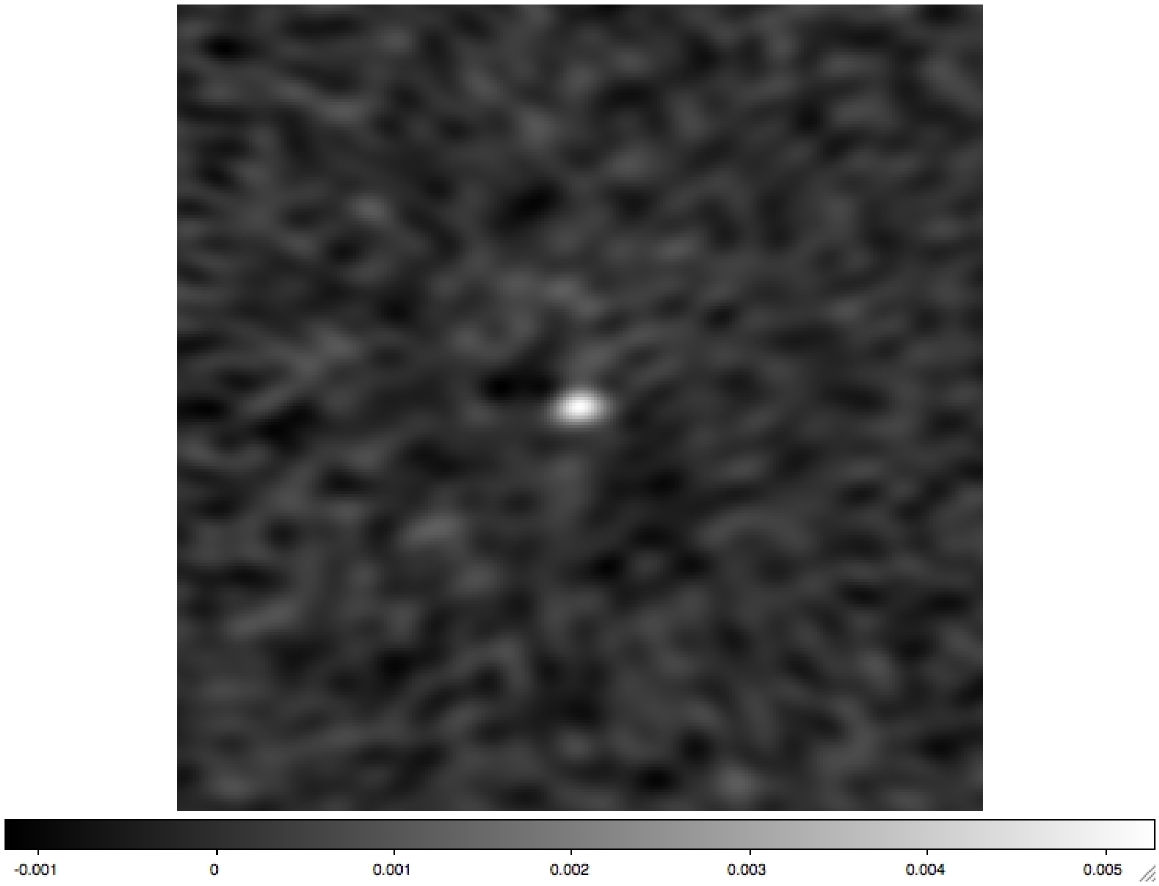

Fig. 41.— CARMA 95 GHz map of 3C186.

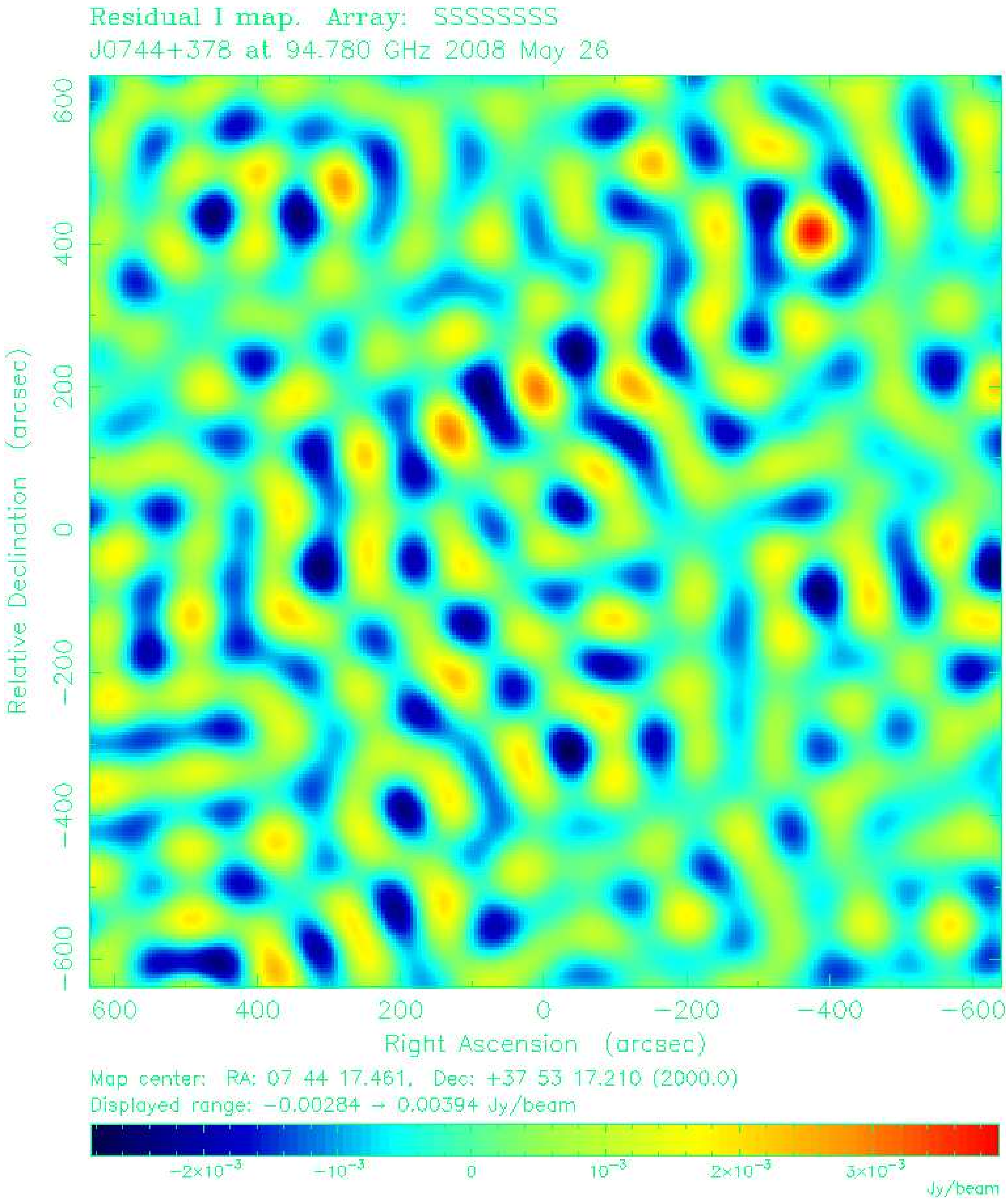

Fig. 42.— SZA 95 GHz map of 3C186, before subtracting the point source from the center.

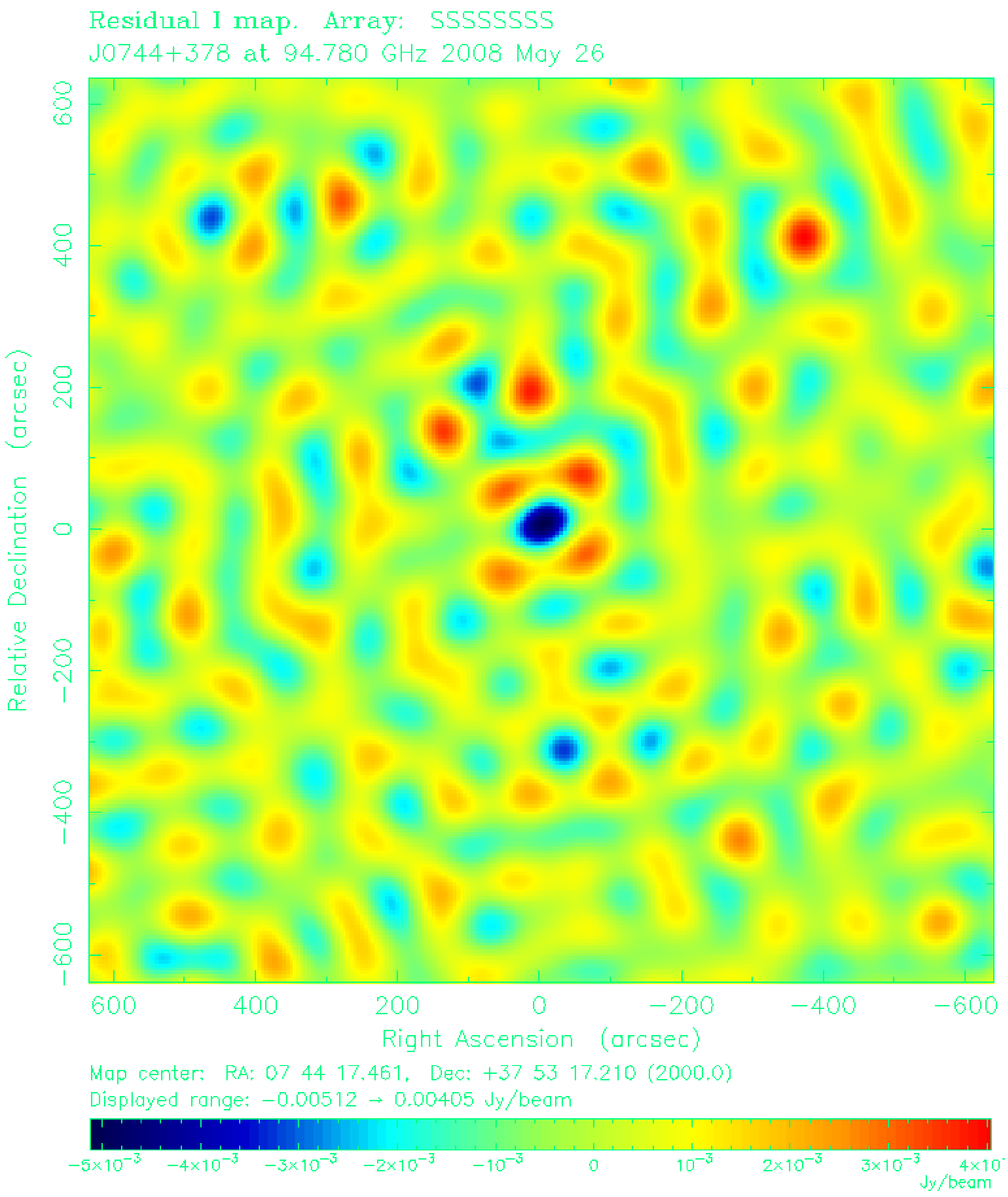

Fig. 43.— SZA 95 GHz map of 3C186, after the 5.5421 mJy point source is modeled and subtracted from the center.

E-mail addresses

Melvyn Wright <wright@astron.berkeley.edu>,
Dick Plambeck <plambeck@astro.berkeley.edu>,
Marc Pound <mpound@astro.umd.edu>,
John Carpenter <jmc@astro.caltech.edu>,
Jin Koda <jkoda@astro.caltech.edu>,
Douglas Bock <dbock@mmarray.org>,
Mike Anderson <michevan@astro.caltech.edu>
Shane Bussmann <rsbussmann@as.arizona.edu>
Joe Converse <jconverse@berkeley.edu>
Stephanie Cortes <scortes@as.arizona.edu>
Timothy Davis <bassist_tim@hotmail.com>
Masayuki Fukuhara <m.fukuhara@nao.ac.jp>
Jithin George <jgeorge@astro.umd.edu>
Josh Goldstein <goldstj@umd.edu>
Sarah Graves <s.graves@mrao.cam.ac.uk>
Nicole Hasler <haslern@uah.edu>
Amanda Heiderman <alh@astro.as.utexas.edu>
David Hogg <hogg@astro.ex.ac.uk>
Katherine Lee <ijlee9@astro.uiuc.edu>
Timothy Morton <tdm@astro.caltech.edu>
Josep-Maria Masque <jmasque@am.ub.es>
Reiko Momose <momo.s.rieko@nao.ac.jp>
Megan Roscioli <roscioli@oddjob.uchicago.edu>
Alvaro Sanchez-Monge <asanchez@am.ub.es>
Dan Welty <welty@oddjob.uchicago.edu>
Lei Zhu <lzhu@cfa.harvard.edu>

REFERENCES

Aikawa Y. et al. 2001, ApJ, 552, 639

Beckwith, S. V. W., Sargent, A. I., Chini, R. S., & Guesten, R. 1990, AJ, 99, 924

Beuther, H., Thorwirth, S., Zhang, Q., Hunter, T. R., Megeath, S. T., et al. 2005, ApJ, 627, 834

Caselli, P., Benson, P. J., Myers, P. C., & Tafalla, M. 2002, ApJ, 572, 238

Carlstrom, J.E., Holder,G.P., & Reese, E.D. ”Cosmology with the Sunyaev-Zel’dovich Effect.” ARA&A, 2002, 40, 643-680.

Furuya, R. S., Kitamura, Y., & Shinnaga, H. 2006, ApJ, 653, 1369

Girart, J.M. et al. 1994, ApJ, 435, L145

Girart, J.M. at al. 1998, ApJ, 495, L59

Girart J.M. et al. 2001, ApJ, 562, L91

Hotzel, S., Harju, J., & Walmsley, C. M. 2004, A&A, 415, 1065

Jijina, J., Myers, P. C. & Adams, F. C. 1999, ApJS, 125, 161

Martí J. et al. 1993, ApJ, 416, 208

Masqué, J.M. et al. 2008, submitted to ApJ

Palau, A., Estalella, R., Girart, J. M., Ho, P. T. P., Zhang, Q., & Beuther, H. 2007, A&A, 465, 219

Rodríguez, L. F. et al. 1980, ApJ, 235, 845

Shu, F. H., Adams, F. C., & Lizano, S. 1987, ARA&A, 25, 23

http://nedwww.ipac.caltech.edu. 2004SDSS2.C...0000

Tafalla, M. et al. 2002, ApJ, 569, 815

Tieftrunk, A. R., Megeath, S. T., Wilson, T. L. & Rayner, J. T. 1998, A&A, 336, 991

Urquhart, J. S., Thompson, M. A., Morgan, L. K., Pestalozzi, M. R., et al. 2007, A&A, 467, 1125

Wu, Y., Henkel, C., Xue, R., Guan, X. & Miller, M. 2007, ApJ, 669, L37